

Spatiotemporal Dynamics, Nowcasting and Forecasting of COVID-19 in the United States

Li Wang^a, Guannan Wang^b, Lei Gao^a, Xinyi Li^c, Shan Yu^d, Myungjin Kim^a,
Yueying Wang^a and Zhiling Gu^a

^aIowa State University, USA, ^bCollege of William & Mary, USA, ^cClemson University, USA
and ^dUniversity of Virginia, USA

Abstract: Epidemic modeling is an essential tool to understand the spread of the novel coronavirus and ultimately assist in disease prevention, policymaking, and resource allocation. In this article, we establish a state of the art interface between classic mathematical and statistical models and propose a novel space-time epidemic modeling framework to study the spatial-temporal pattern in the spread of infectious disease. We propose a quasi-likelihood approach via the penalized spline approximation and alternatively reweighted least-squares technique to estimate the model. Furthermore, we provide a short-term and long-term county-level prediction of the infected/death count for the U.S. by accounting for the control measures, health service resources, and other local features. Utilizing spatiotemporal analysis, our proposed model enhances the dynamics of the epidemiological mechanism and dissects the spatiotemporal structure of the spreading disease. To assess the uncertainty associated with the prediction, we develop a projection band based on the envelope of the bootstrap forecast paths. The performance of the proposed method is evaluated by a simulation study. We apply the proposed method to model and forecast the spread of COVID-19 at both county and state levels in the United States.

Key words and phrases: Coronavirus; nonparametric modeling; partially linear models; spatial epidemiology; splines; varying coefficient models.

1 Background & Introduction

The severe acute respiratory syndrome coronavirus 2 (SARS-CoV-2) outbreak started last December, and it has expanded to impact nearly every corner of the world. On the New Year's Eve of 2019, the World Health Organization (WHO) was informed mysterious pneumonia cases in Wuhan, China. On January 3, 2020, 44 cases were reported to WHO, among whom 11 were severely ill (WHO, 2020b). By February 4, confirmed cases had been reported in 24 countries outside China (WHO, 2020d). The US confirmed its first case in Washington state On January 21 – a man who returned to the US from Wuhan (CDC, 2020b). On January 30, the US Centers for Disease Control and Prevention (CDC) confirmed the person-to-person spread of coronavirus in the US (CDC, 2020). On the same day, the WHO declared the coronavirus outbreak as a Public Health Emergency of International Concern (WHO, 2020c,e).

Address for correspondence: Li Wang (lilywang@iastate.edu)

Many nonpharmaceutical interventions (NPIs) were implemented to prevent the spread of COVID-19. For example, Wuhan implemented screening measures for travelers leaving the city at airports, railway stations, and other passenger terminals, and eventually closed off Wuhan City on January 22 (Qin and Wang, 2020). The US started screening at twenty airports at the end of January (Aratani and Berger, 2020). On February 25, San Francisco became the first US city to declare a state of emergency over COVID-19 (State of the City and County of San Francisco, 2020), followed by the states of Washington (State of Washington, Office of the Governor, 2020) and Florida (State of Florida, Office of the Governor, 2020). On March 13, President Donald Trump declared a national COVID-19 emergency (TRUMP, 2020), and sixteen states announced school closures by then (Ujifusa, 2020). On March 19, California issued a “stay-at-home” order for all of its 40 million residents (Karimi and Moon, 2020), and within two weeks, the majority of the states had taken similar actions. By the end of March, more than 91% of the world’s population lived in countries with restrictions for non-resident travelers from abroad (Phillip Connor, 2020).

Even with all the control measures taken in place, the spread of COVID-19 is still dramatic. From February 7 to 14, both the total cases confirmed and deaths worldwide almost doubled within one week. Meanwhile, COVID-19 kept spreading globally, and over 50 countries reported confirmed cases by the end of February (WHO, 2020a). During mid-March, COVID-19 presented in all 50 states in the US. Starting from March 26, the US led the world in COVID-19 cases. On May 28, the US COVID-19 death count passed one hundred thousand, and then in the middle of June, the number of confirmed cases of COVID-19 hit two million in the US. The confirmed and death cases kept increasing rapidly in the following months. By the beginning of September, the US surpassed six million confirmed cases and hit seven million on September 25. On October 16, the US surpassed eight million confirmed cases and 218 thousand deaths (CDC, 2020).

The effect of COVID-19 is profound. The World Bank estimated that the coronavirus pandemic could push additional 16 million people into extreme poverty. On April 14, the International Monetary Fund warned that the world is facing its worst economic downturn as coronavirus lockdowns continue to wreak havoc on the global economy (Gopinath, 2020). Due to the immense pressures of the crippled economy and an anxious public amid a pandemic, the US started to loosen lockdown measures in late April and backtracked after reopening for a few weeks and seeing a surge in cases. As the pandemic progresses, there are broader interests from the public in answering questions such as how far the SARS-CoV-2 virus will spread, how many lives it will eventually claim, how effective intervention strategies will be, as well as whether and when the pandemic will resurge.

Epidemic modeling is an important scientific tool to answer these questions by aiding people to understand the pandemic data, make predictions, and help the medical professionals and decision-

makers allocate resources and design/evaluate intervention strategies to fight against COVID-19; see Gog (2020); Vespignani et al. (2020). Several attempts had been made to model and forecast the spread and mortality of COVID-19; for example, see Kucharski et al. (2020); Sun et al. (2020).

The fundamental concept of infectious disease epidemiology is investigating how the diseases spread. Mathematical models are undeniably useful in understanding the dynamics of infectious disease spread Keeling and Rohani (2008). An essential type of mathematical model is the class of mechanistic models such as the Susceptible-Infectious-Removed (SIR) compartmental model or the Susceptible-Exposed-Infectious-Recovered model (SEIR); see details in Brauer et al. (2008); Lawson et al. (2016). Mechanistic models make explicit hypotheses about the biological mechanisms that drive the dynamics of infection. These mechanistic models characterize disease transmission through a set of differential equations, and they demonstrate the average behavior of the epidemic. Statistical modeling is another powerful tool for extracting information about the disease spread in epidemic studies Held et al. (2020). The data modeling is one of the cultures in statistical modeling, it is usually designed for inference about the relationships between variables whilst also catering to prediction. When analyzing the confirmed cases and deaths of COVID-19, other factors, such as demographics, socioeconomic status, mobility, and control policies, may also be responsible for temporal or spatial patterns. For maximal effectiveness, we create a novel method to appreciate and exploit the complementary strengths of mathematical and statistical models in this paper.

We borrow the mechanistic rules from the SIR model and form a data-driven model with three compartments: infectious, susceptible, and removed states. The capacity of the health care system, and control measures, such as government-mandated social distancing, also have a significant impact on the spread of the epidemic. We borrow the strength from statistical models and include various explanatory variables to study not only the spatiotemporal structure but also the effects of the explanatory variables. Notice that the spread of the disease varies a lot across different geographical regions; we incorporate discrete-time spatially varying coefficient models to different compartments to reconstruct the spatiotemporal dynamics of the disease transmission. In general, the spatiotemporal models are able to bring in more information to the epidemic study (Held et al., 2019; Jia et al., 2020).

With an emerging disease such as COVID-19, it is hard to measure many features of the transmission process, which may take a long time to fully understand. Thus, it is desirable to make inferences from observed data as model-free as possible. For a parametric epidemic model, the typical inference problem involves estimating the parameters associated with the parametric models from the data at hand. Such specifications are ad hoc, and if misspecified, can lead to substantial estimation bias problems. This issue might be addressed in practice by considering alternative nonparametric models or sensitivity analyses if some of the underlying model parameters are assumed to be known. By adopting

a nonparametric approach, we do not impose a particular parametric structure, which significantly enhances the flexibility of the parametric epidemic models. Nonparametric approaches to fitting epidemic models to the data have received relatively little attention in the literature, possibly due to the lack of data. With the rich COVID-19 epidemic data released every day, we can consider the nonparametric method to model the covariates and coefficient functions.

By allowing the response (such as infected and death counts) to depend on time and location, we consider a generalized additive varying coefficient model to estimate the unobserved process of the disease transmission. For our model estimation, we propose a quasi-likelihood approach via the penalized spline approximation and an iteratively reweighted least-squares technique. Our proposed algorithm is sufficiently fast and efficient for the user to analyze large datasets within seconds. As an empirical illustration, we apply the proposed model and estimation method to a study of COVID-19 at the county-level in the US. We illustrate how the proposed method can be used to analyze the spatiotemporal dynamics of the disease spread and guide evidence-based decision making.

Finally, prediction models for COVID-19 at the county-level that combine local characteristics and actions are very beneficial for the community to understand the dynamics of the disease spread and support decision making at a time when they are urgently needed. Knowing more about the vulnerable communities and the reasons for those communities that are more likely to be infected are crucial for the policy and decision-makers to assist in prevention efforts and ultimately stop the pandemic. In this paper, we consider both the short-term impact and long-term impact of the SARS-CoV-2 virus at the county level in the U.S. To assess the uncertainty associated with the prediction, we also propose a projection band constructed based on the envelope of the bootstrap forecast paths, which are closest to the forecast path obtained based on the original sample.

The rest of the paper is organized as follows. Section 2 presents the epidemic and endemic data. Section 3 outlines the nonparametric spatiotemporal modeling framework and describes how to incorporate additional covariates. Section 4 introduces our estimation method, our algorithm and details of the implementation. Section 5 provides the prediction as well as the uncertain quantification with the prediction band of the forecast path. Section 6 evaluates the finite sample performance of the proposed method using a simulation study. Section 7 describes the results and findings of the case study. Section 8 concludes the paper with a discussion. Supplementary Material (<https://faculty.sites.iastate.edu/lilywang/arxiv>) contains some animation videos of the dynamic estimation results in the COVID-19 study.

2 COVID-19 Case Study and Data

2.1 Research Goal of the Study

The goal of this study is threefold. First, we develop a new dynamic epidemic modeling framework for public health surveillance data to study the spatial-temporal pattern in the spread of COVID-19. We aim to investigate whether the proposed model could be used to guide the modeling of the dynamic of the spread at the county level by moving beyond the typical theoretical conceptualization of context where a county's infection is only associated with its own features. Second, to understand the factors that contribute to the spread of COVID-19, we model the daily infected cases at the county level in consideration of the demographic, environmental, behavioral, socioeconomic factors in the U.S. Third, we project the spatial-temporal pattern of the spread of the virus in the U.S. For the short-term forecast, we provide the prediction of the daily infection count and death count up to the county level. As for the long-term forecast, we project the total infected and death cases in the next three months.

2.2 Epidemic Data from the COVID-19 Outbreak in the U.S.

This study analyzes data from the reported confirmed COVID-19 infections and deaths at the county level, which are reported by the 3,104 counties from the 48 mainland U.S. states and the District of Columbia. The aggregated COVID-19 cases are from January 20 until September 3, 2020. The data are collected, compiled and cleaned from a combination of public sources that aim to facilitate the research effort to confront COVID-19, including Health Department Website in each state or region, the New York Times (NYT, 2020), the COVID-19 Data Repository by the Center for Systems Science and Engineering at Johns Hopkins University (JHU CSSE, 2020), and the COVID Tracking Project (Atlantic, 2020). These data sources automatically updated every day or every other day. We have created a dashboard <https://covid19.stat.iastate.edu/> to visualize and track the infected and death cases, which was launched on March 27, 2020.

2.3 Information of the covariates

We consider various county-level characteristics as covariate information in our study, which can be divided into six groups. The data sources and the operational definitions of these features are discussed as follows, and a list of all the variables is summarized in Table 2.1.

Policies. Government declarations are used to identify the dates that different jurisdictions implemented various social distancing policies (emergency declarations, school closures, bans on large gatherings, limits on bars, restaurants and other public places, the deployment of severe travel restrictions, and “stay-at-home” or “shelter-in-place” orders). President Trump declared a state of emergency on March 13, 2020, to enhance the federal government response to confront the COVID-19. By March

16, 2020, every state had made an emergency declaration. Since then, more severe social distancing actions had been taken by the majority of the states, especially those hardest hit by the pandemic. We compiled the dates of executive orders by checking national and state governmental websites, news articles and press releases.

Demographic Characteristics. To capture the demographic characteristics of a county, five variables are considered in the analysis to describe the racial, ethnic, sexual and age structures: the percent of the population who identify as African American, the percent of the population who identify as Hispanic or Latino, the rate of aged people (≥ 65 years) per capita, the ratio of male over female and population density over square mile of land area. The former two variables were obtained from the 2010 Census (U.S. Census Bureau, 2010), and the latter three variables are extracted from the 2010–2018 American Community Survey (ACS) Demographic and Housing Estimates (U.S. Census Bureau, 2010).

Healthcare Infrastructure. We incorporated three components in our analysis to describe the healthcare infrastructure in each county: percent of the population aged less than 65 years without health insurance, local government expenditures for health per capita, and total counts of hospital beds per 1,000 population. These components measure the access for residents to public health resources within and across counties. The first component is available in the USA Counties Database (U.S. Census Bureau, 2010), the second is from Economic Census 2012 (U.S. Census Bureau, 2012), and the last is compiled from Homeland Infrastructure Foundation-level Data (U.S. Department of Homeland Security).

Socioeconomic Status. A diverse of factors are considered to describe the socioeconomic status in each county. We first apply the factor analysis to seven factors collected from the 2005–2009 ACS 5-year estimates (U.S. Census Bureau, 2010), and generate two factors: social affluence and concentrated disadvantage. To be specific, the former is comprised of the percent of families with annual incomes higher than \$75,000 (factor loading = 0.86), percent of the population aged 25 years or older with a bachelor's degree or higher (factor loading = 0.92), percent of the people working in management, professional, and related occupations (factor loading = 0.73), and the median value of owner-occupied housing units (factor loading = 0.74); whereas the latter includes the percent of the households with public assistance income (factor loading = 0.34), the percent of households with female householders and no husband present (factor loading = 0.81), and civilian labor force unemployment rate (factor loading = 0.56). These two factors, affluence and disadvantage, explain more than 60% of the variation.

We also incorporate the Gini coefficient to measure income inequality. The Gini coefficient, also known as Gini index, is a well-known measure for income inequality and wealth distribution in economics, with value ranging from zero (complete equality, where everyone has exactly the same income)

to one (total inequality, where one person occupies all of the income). The 2005–2009 ACS (U.S. Census Bureau, 2010) provided the household income data that allow us to calculate the Gini coefficient.

Rural/urban Factor. In the literature, rural/urban residence has been found to be associated with the spread of epidemics. Specifically, rural counties are often characterized by poor socio-economic profiles and limited access to healthcare services, indicating a potential higher risk. To capture rural/urban residence, we use the urban rate from the 2010 Census (U.S. Census Bureau, 2010).

Geographic Information. The longitude and latitude of the geographic center for each county in the U.S. are available in Gazetteer Files (U.S. Census Bureau, 2019).

Mobility. The data are collected and cleaned from U.S. Department of Transportation, Bureau of Transportation Statistics and Descartes Labs. It describes the daily number of trips within each county produced from an anonymized national panel of mobile device data from multiple sources. Trips are defined as movements that include a stay of longer than 10 minutes at an anonymized location away from home.

3 Space-time Epidemic Modeling

In this section, to study the spatiotemporal pattern of COVID-19, we developed a novel spatiotemporal epidemic model (STEM) to estimate and predict the infection and death cases at the area level based on the idea of the compartment models. For simplicity, we introduce the STEM based on the parsimonious SIR models, but it can be extended to the SEIR models with an extra “exposed” compartment for infected but not infectious individuals.

For area i and day t , let Y_{it} be the number of new cases, and let I_{it} , D_{it} , R_{it} , and S_{it} be the number of accumulated active infectious cases, accumulated death cases, accumulated recovered cases, and susceptible population, respectively. Let N_i be the total population for the i th area, and denote $Z_{it} = \log(S_{it}/N_i)$. Let $\mathbf{U}_i = (U_{i1}, U_{i2})^\top$ be the GPS coordinates of the geographic center of area i , which ranges over a bounded domain $\Omega \subseteq \mathbb{R}^2$ of the region under study. Let $\mathbf{X}_i = (X_{i1}, \dots, X_{iq})^\top$ be a q -dimensional vector of explanatory variables collected from the U.S. Census Bureau. For example, the socioeconomic factors, health resources, and demographic conditions. Let A_{ijt} be the j th dummy variable of actions or measures taken for area i at time t , and let $\mathbf{A}_{it} = (A_{i1t}, \dots, A_{ipt})^\top$, which varies with the time.

In this paper, we consider the exponential families of distributions. The conditional density of Y_{it} given $(I_{i-1}, Z_{i,t-1}, \mathbf{A}_{i,t-r}, \mathbf{X}_i, \mathbf{U}_i) = (w, z, \mathbf{a}, \mathbf{x}, \mathbf{u})$ can be represented as

$$f(y|w, z, \mathbf{a}, \mathbf{x}, \mathbf{u}) = \exp \left[\frac{1}{\sigma^2} \{y\zeta(w, z, \mathbf{a}, \mathbf{x}, \mathbf{u}) - \mathcal{B}\{\zeta(w, z, \mathbf{a}, \mathbf{x}, \mathbf{u})\}\} + \mathcal{C}(y, \sigma^2) \right],$$

for some known functions \mathcal{B} and \mathcal{C} , dispersion parameter σ^2 and the canonical parameter ζ .

Table 2.1: County-level characteristics (predictors) used in the modeling.

Predictors	Description
Control	Dummy variable for declaration of “shelter-in-place” or “stay-at-home” order (Control = 1, for “shelter-in-place”, and Control = 0, for no restriction or restriction lifted)
Socioeconomic Status	
Affluence	Social affluence
Disadvantage	Concentrated disadvantage
Gini	Gini coefficient
Healthcare Infrastructure	
NHIC	Percent of persons under 65 years without health insurance
EHPC	Local government expenditures for health per capita
TBed*	Total bed counts per 1000 population
Demographic Characteristics	
AA	Percent of African American population
HL	Percent of Hispanic or Latino population
PD*	Population density per square mile of land area
Old	Aged people (age ≥ 65 years) rate per capita
Sex	Ratio of male over female
Environment Characteristics	
Mobility	Daily number of trips within each county
Urban	Urban rate

Note: The covariates with * represent that they are transformed from the original value by $f(x) = \log(x + \delta)$. For example, $PD^* = \log(PD + \delta)$, where δ is a small number.

We assume that the determinants of the daily new cases of a particular area can be explained not only by the features of that area but also by the characteristics of the surrounding areas. Based on the idea of the SIR models, we propose a discrete-time spatial epidemic model comprising the susceptible state, infected state, removed state, and area-level characteristics. Below we use superscripts I, D and R to denote infected, death and recovered states. We assume that the conditional mean value of daily new positive cases (μ_{it}^I), fatal cases (μ_{it}^D) and recovery (μ_{it}^R) in area i and day t can be modeled via a link function g as follows:

$$g(\mu_{it}^I) = \beta_{0t}^I(\mathbf{U}_i) + \beta_{1t}^I(\mathbf{U}_i) \log(I_{i,t-1}) + \alpha_{0t}^I Z_{i,t-1} + \sum_{j=1}^p \alpha_{jt}^I A_{ij,t-r} + \sum_{k=1}^q \gamma_{kt}^I(X_{ik}), \quad (3.1)$$

$$g(\mu_{it}^D) = \beta_{0t}^D(\mathbf{U}_i) + \beta_{1t}^D \log(I_{i,t-\delta}) + \sum_{j=1}^p \alpha_{jt}^D A_{ij,t-r'} + \sum_{k=1}^q \gamma_{kt}^D(X_{ik}), \quad (3.2)$$

$$\mu_{it}^R = \nu_t^R I_{i,t-\delta'}, \quad (3.3)$$

where α_{jt}^I 's, α_{jt}^D 's, β_{1t}^D and ν_t^R are unknown constant coefficients, $\beta_{0t}^I(\cdot)$, $\beta_{1t}^I(\cdot)$, and $\beta_{0t}^D(\cdot)$ are unknown bivariate coefficient functions, $\gamma_{kt}^I(\cdot)$, $\gamma_{kt}^D(\cdot)$, $k = 1, \dots, q$, are univariate functions to be estimated, δ and δ' are the time delay between illness and death or recovery, and the parameter r in $A_{ij,t-r}$'s denotes a small delay time allowing for the control measure to be effective (here we take $r = 7$, $r' = 7$). For model identifiability, we assume $E(\gamma_{kt}^I) = 0$, $E(\gamma_{kt}^D) = 0$, $k = 1, \dots, q$. The STEM encompasses many existing models as special cases. For example, the traditional generalized linear regression models, generalized additive models (Liu et al., 2013), generalized partially linear additive models (Wang et al., 2011) and generalized additive coefficient model (Xue and Liang, 2010).

Note that, for the log link, $\exp\{\beta_{0t}^I(\mathbf{u})\}$ illustrates the transmission rate at location \mathbf{u} , $\exp\{\beta_{0t}^D(\mathbf{u})\}$ represents the fatality rate at location \mathbf{u} , ν_t^R is the recovery rate, $\beta_{1t}^I(\cdot)$, α_{0t}^I and β_{1t}^D are the mixing parameters of the contact process. The rationale for including $\beta_{1t}^I(\cdot)$ and β_{1t}^D ($\beta_{1t}^I(\cdot) > 0$, $\beta_{1t}^D > 0$) is to allow for deviations from mass action and to account for the discrete-time approximation to the continuous time model (Finkenstädt and Grenfell, 2000; Wakefield et al., 2019). In many cases, the standard bilinear form may not necessarily hold. The above proposed epidemic model incorporates the nonlinear incidence rates, which represents a much wider range of dynamical behavior than those with bilinear incidence rates (Liu et al., 1987). These dynamical behaviors are determined mainly by $\beta_{0t}^I(\cdot)$, $\beta_{1t}^I(\cdot)$, $\beta_{0t}^D(\cdot)$, and β_{1t}^D . For example, when $\beta_{1t}^I(\cdot)$ and α_{0t}^I are both 1, it corresponds to the standard assumption of homogeneous mixing in De Jong et al. (1995).

In our study, since we model the number of new cases at time t for area i , Poisson or Negative Binomial (NB) might be an appropriate option for random component (Kim and Wang, 2020; Yu et al., 2020). For example, for the infection model, we can assume that

- (Poisson) $E(Y_{it}|Z_{i,t-1}, \mathbf{A}_{i,t-r}, \mathbf{X}_i, \mathbf{U}_i) = \mu_{it}^I$, $\text{Var}(Y_{it}|Z_{i,t-1}, \mathbf{A}_{i,t-r}, \mathbf{X}_i, \mathbf{U}_i) = \mu_{it}^I$,
- (NB) $E(Y_{it}|Z_{i,t-1}, \mathbf{A}_{i,t-r}, \mathbf{X}_i, \mathbf{U}_i) = \mu_{it}^I$, $\text{Var}(Y_{it}|Z_{i,t-1}, \mathbf{A}_{i,t-r}, \mathbf{X}_i, \mathbf{U}_i) = \mu_{it}^I(1 + \mu_{it}^I/I_{i,t-1})$,

where μ_{it}^I can be modeled via the same log link as follows:

$$\log(\mu_{it}^I) = \beta_{0t}^I(\mathbf{U}_i) + \beta_{1t}^I(\mathbf{U}_i) \log(I_{i,t-1}) + \alpha_{0t}^I Z_{i,t-1} + \sum_{j=1}^p \alpha_{jt}^I A_{ij,t-r} + \sum_{k=1}^q \gamma_{kt}^I(X_{ik}). \quad (3.4)$$

We can consider similar models for the death count. At the beginning of the outbreak, infected and death cases could be rare, so ‘‘Poisson’’ might be a reasonable choice of the random component to describe the distribution of rare events in a large population. As the disease progresses, the variation of infected/death count increases across counties and states. So, at the acceleration phase of the disease, the negative binomial random component might be an appropriate option for the presence of over-dispersion.

The above spatiotemporal epidemic model (STEM) is developed based on the foundation of epidemic modeling. It can provide a rich characterization of different types of errors for modeling the uncertainty. Moreover, it accounts for both spatiotemporal nonstationarity and area-level local features simultaneously. It also offers flexibility in assessing the dynamics of the spread at different times and locations than various parametric models in the literature.

4 Estimation of the STEM

In this section, we describe how to estimate the parameters and nonparametric components in the proposed STEM model. To capture the temporal dynamics, we consider the moving window approach.

4.1 Penalized Quasi-likelihood Method

We first describe the estimation of model (3.1). For the current time t , and roughness parameters λ_0 and λ_1 , we consider the penalized quasi-likelihood problem defined as follows:

$$\sum_{i=1}^n \sum_{s=t-t_0}^t L \left[g^{-1} \left\{ \beta_0(\mathbf{U}_i) + \beta_1(\mathbf{U}_i) \log(I_{i,s-1}) + \alpha_0 Z_{i,s-1} + \sum_{j=1}^p \alpha_{jt} A_{ij,s-r} + \sum_{k=1}^q \gamma_{kt}(X_{ik}) \right\}, Y_{is} \right] - \frac{1}{2} \{ \lambda_0 \mathcal{E}(\beta_0) + \lambda_1 \mathcal{E}(\beta_1) \}, \quad (4.1)$$

where $t_0 + 1$ is the window width for the model fitting, and it can be selected by minimizing the prediction errors or maximizing the correlation between the predicted and observed values. The energy functional is defined as follows:

$$\mathcal{E}(\beta) = \int_{\Omega} \{ (\nabla_{u_1}^2 \beta)^2 + 2(\nabla_{u_1} \nabla_{u_2} \beta)^2 + (\nabla_{u_2}^2 \beta)^2 \} du_1 du_2, \quad (4.2)$$

where $\nabla_{u_j}^q \beta(\mathbf{u})$ is the q th order derivative in the direction u_j , $j = 1, 2$, at any location $\mathbf{u} = (u_1, u_2)^\top$.

Note that, except for parameters $\{\alpha_j\}_{j=0}^p$, other functions are related to curse of dimensionality due to the nature of functions. To handle this difficulty, we employ the basis expansion approach to approximate the univariate and bivariate functions discussed below. The univariate additive components $\{\gamma_k(\cdot)\}_{k=1}^q$ and the spatially varying coefficient components $\{\beta_\ell(\cdot)\}_{\ell=0}^1$ in model (3.4) are approximated using univariate polynomial spline and bivariate penalized splines over triangulation (BPST), respectively. The BPST method is well known to be computationally efficient to deal with data distributed on complex domains with irregular shape or with holes inside; see the details in Lai and Wang (2013) and Sangalli et al. (2013). We provide a brief introduction to univariate and bivariate splines below. Assume that X_k takes value on an interval $[a_k, b_k]$, $k = 1, \dots, q$. Let $\mathcal{U}_k = \mathcal{U}_k^\varrho([a_k, b_k])$ be the space of the polynomial splines of order $\varrho + 1$. Next, let $\mathcal{U}_k^0 = \{\phi \in \mathcal{U}_k : E\phi(X_k) = 0\}$, which creates a space of the centered spline functions; see Xue and Liang (2010), Liu et al. (2013) and Wang et al. (2020c). Let \mathcal{J} be the index set of the basis functions, and then denote by $\{\varphi_{kJ}(x_k), J \in \mathcal{J}\}$ the original B-spline basis functions for the k th covariate. Let $\varphi_{kJ}^0(x_k) = \varphi_{kJ}(x_k) - \varphi_{k1}(x_k)E\varphi_{kJ}(X_k)/E\varphi_{k1}(X_k)$, $\Phi_{kJ}(x_k) = \varphi_{kJ}^0(x_k)/SD\{\varphi_{kJ}^0(X_k)\}$, $J \in \mathcal{J}$, then $E\Phi_{kJ}(X_k) = 0$ and $E\Phi_{kJ}^2(X_k) = 1$. For all $x_k \in [a_k, b_k]$, the estimator of $\gamma_k(x_k)$ is $\hat{\gamma}_k(x_k) = \sum_{J \in \mathcal{J}} \xi_{kJ} \Phi_{kJ}(x_k) = \mathbf{\Phi}_k^\top(x_k) \boldsymbol{\xi}_k$, where $\mathbf{\Phi}_k(x_k) = (\Phi_{kJ}(x_k), J \in \mathcal{J})^\top$ and $\boldsymbol{\xi}_k = (\xi_{kJ}, J \in \mathcal{J})^\top$ is a vector of coefficients.

For the bivariate coefficient functions $\beta_0(\cdot)$ and $\beta_1(\cdot)$ in the STEM model (3.4), we introduce bivariate spline over triangulation (Lai and Wang, 2013). The spatial domain Ω with either an arbitrary shape or holes inside can be partitioned into M triangles, T_1, \dots, T_M , that is, $\Omega = \cup_{m=1}^M T_m$. Then, denote $\Delta := \{T_1, \dots, T_M\}$ by a triangulation of the domain Ω (Lai and Schumaker, 2007); see, for example, Figure 6.3. Given an integer $d \geq 0$, let $\mathbb{P}_d(T)$ be the space of all polynomials of degree $\leq d$ on T . Let $\mathbb{C}^r(\Omega)$ be the space of r th continuously differentiable functions over the domain Ω . For $0 \leq r < d$ and Δ , we construct the spline space of degree d and smoothness r over Δ in the following:

$$\mathbb{S}_d^r(\Delta) = \{\mathcal{P} \in \mathbb{C}^r(\Omega) : \mathcal{P}|_{T_m} \in \mathbb{P}_d(T_m), T_m \in \Delta, m = 1, \dots, M\}. \quad (4.3)$$

For triangulation Δ with M triangles, denote a set of bivariate Bernstein basis polynomials for $\mathbb{S}_d^r(\Delta)$ as $\{B_m(\mathbf{u})\}_{m \in \mathcal{M}}$, where an index set \mathcal{M} for basis functions has its cardinality $|\mathcal{M}| = M(d+1)(d+2)/2$. Then, we can approximate the bivariate functions $\beta_\ell(\cdot) \in \mathbb{S}_d^r(\Delta)$ in the STEM model (3.4) by $\sum_{m \in \mathcal{M}} B_m(\mathbf{u}) \theta_{\ell m} = \mathbf{B}(\mathbf{u})^\top \boldsymbol{\theta}_\ell$, where $\mathbf{B}(\mathbf{u}) = \{B_m(\mathbf{u}), m \in \mathcal{M}\}^\top$ and $\boldsymbol{\theta}_\ell = \{\theta_{\ell m}, m \in \mathcal{M}\}^\top$.

In practice, the triangulation can be obtained through varieties of software; see for example, the ‘‘Delaunay’’ algorithm (*delaunay.m* in MATLAB or *DelaunayTriangulation* in MATHEMATICA), the R package ‘‘Triangulation’’ (Wang and Lai, 2019), and the ‘‘DistMesh’’ Matlab code. The bivariate spline basis are generated via the R package ‘‘BPST’’ (Wang et al., 2019). See more discussions of how to generate the bivariate spline over triangulations in Mu et al. (2018) and Yu et al. (2020).

Considering the basis expansion, the energy functional $\mathcal{E}(\beta_\ell)$ in (4.2) can be approximated by $\mathcal{E}(\mathbf{B}(\cdot)^\top \boldsymbol{\theta}_\ell) = \boldsymbol{\theta}_\ell^\top \mathbf{P} \boldsymbol{\theta}_\ell$, for $\ell = 0, 1$, where \mathbf{P} is a block diagonal penalty matrix. By introducing the constraint matrix \mathbf{H} which satisfies $\mathbf{H} \boldsymbol{\theta}_\ell = \mathbf{0}$, $\ell = 0, 1$, we can reflect global smoothness in $\mathbb{S}_d^r(\Delta)$ in (4.3). For the current time t , the maximization problem (4.1) is changed to minimize

$$\begin{aligned} & - \sum_{i=1}^n \sum_{s=t-t_0}^t L \left(g^{-1} \left[\mathbf{B}(\mathbf{U}_i)^\top \{ \boldsymbol{\theta}_0 + \boldsymbol{\theta}_1 \log(I_{i,s-1}) \} + \alpha_0 Z_{i,s-1} + \sum_{j=1}^p \alpha_j A_{ij,s-r} \right. \right. \\ & \left. \left. + \sum_{k=1}^q \boldsymbol{\Phi}_k^\top (X_{ik}) \boldsymbol{\xi}_k \right], Y_{is} \right) + \frac{1}{2} (\lambda_0 \boldsymbol{\theta}_0^\top \mathbf{P} \boldsymbol{\theta}_0 + \lambda_1 \boldsymbol{\theta}_1^\top \mathbf{P} \boldsymbol{\theta}_1) \quad \text{subject to } \mathbf{H} \boldsymbol{\theta}_\ell = \mathbf{0}, \ell = 0, 1. \end{aligned} \quad (4.4)$$

Directly solving the optimization problem in (4.4) is not straightforward due to the smoothness constraints involved. Instead, suppose that the rank r matrix \mathbf{H}^\top is decomposed into $\mathbf{Q}\mathbf{R} = (\mathbf{Q}_1 \mathbf{Q}_2) \begin{pmatrix} \mathbf{R}_1 \\ \mathbf{R}_2 \end{pmatrix}$, where \mathbf{Q}_1 is the first r columns of an orthogonal matrix \mathbf{Q} , and \mathbf{R}_2 is a matrix of zeros, which is a sub-matrix of an upper triangle matrix \mathbf{R} . Then, reparametrization of $\boldsymbol{\theta}_\ell = \mathbf{Q}_2 \boldsymbol{\theta}_\ell^*$ for some $\boldsymbol{\theta}_\ell^*$, $\ell = 0, 1$, enforces $\mathbf{H} \boldsymbol{\theta}_\ell = \mathbf{0}$. Thus, the constraint problem in (4.4) can be changed to an unconstrained optimization problem as follows:

$$\begin{aligned} & - \sum_{i=1}^n \sum_{s=t-t_0}^t L \left(g^{-1} \left[\mathbf{B}(\mathbf{U}_i)^\top \mathbf{Q}_2 \{ \boldsymbol{\theta}_0^* + \boldsymbol{\theta}_1^* \log(I_{i,s-1}) \} + \alpha_0 Z_{i,s-1} + \sum_{j=1}^p \alpha_j A_{ij,s-r} \right. \right. \\ & \left. \left. + \sum_{k=1}^q \boldsymbol{\Phi}_k^\top (X_{ik}) \boldsymbol{\xi}_k \right], Y_{is} \right) + \frac{1}{2} \left(\lambda_0 \boldsymbol{\theta}_0^{*\top} \mathbf{Q}_2^\top \mathbf{P} \mathbf{Q}_2 \boldsymbol{\theta}_0^* + \lambda_1 \boldsymbol{\theta}_1^{*\top} \mathbf{Q}_2^\top \mathbf{P} \mathbf{Q}_2 \boldsymbol{\theta}_1^* \right). \end{aligned} \quad (4.5)$$

Let $(\hat{\boldsymbol{\theta}}_{0t}^*, \hat{\boldsymbol{\theta}}_{1t}^*)^\top$, $(\hat{\alpha}_{0t}, \hat{\alpha}_{1t}, \dots, \hat{\alpha}_{pt})^\top$, and $(\hat{\boldsymbol{\xi}}_{1t}, \dots, \hat{\boldsymbol{\xi}}_{qt})^\top$ be the minimizers of (4.5) at time point t . Then, the estimator of $\beta_{\ell t}(\cdot)$ is $\hat{\beta}_{\ell t}(\mathbf{u}) = \mathbf{B}(\mathbf{u})^\top \mathbf{Q}_2 \hat{\boldsymbol{\theta}}_{\ell t}^*$, $\ell = 0, 1$, the estimator of α_{jt} is $\hat{\alpha}_{jt}$, $j = 1, \dots, p$, and the spline estimator $\gamma_{kt}(\cdot)$ is $\hat{\gamma}_{kt}(x_k) = \boldsymbol{\Phi}_k(x_k)^\top \hat{\boldsymbol{\xi}}_{kt}$, $k = 1, \dots, q$.

4.2 Penalized Iteratively Reweighted Least Squares Algorithm

We now describe the estimating algorithm in detail. For the current time t , let $\mathbf{Y} = (\mathbf{Y}_1^\top, \dots, \mathbf{Y}_t^\top)^\top$ be the vector of the responses where $\mathbf{Y}_s = (Y_{1s}, \dots, Y_{ns})^\top$. Denote $\boldsymbol{\Phi}_i^\top = \{ \boldsymbol{\Phi}_1(X_{i1})^\top, \dots, \boldsymbol{\Phi}_q(X_{iq})^\top \}$, $\mathbf{A}_{is}^\top = (A_{i1,s-r}, \dots, A_{ip,s-r})$, and $\mathbf{F} = (\mathbf{F}_1, \dots, \mathbf{F}_t)^\top$, where $\mathbf{F}_s = (\mathbf{F}_{1s}, \dots, \mathbf{F}_{ns})$, and $\mathbf{F}_{is}^\top = (\mathbf{A}_{is}^\top, \boldsymbol{\Phi}_i^\top, [\{1, \log(I_{i,s-1})\}^\top \otimes \{\mathbf{Q}_2^\top \mathbf{B}(\mathbf{U}_i)\}^\top])$. Denote $\boldsymbol{\vartheta} = (\boldsymbol{\alpha}^\top, \boldsymbol{\xi}^\top, \boldsymbol{\theta}^{*\top})^\top$, and let $\eta_{is}(\boldsymbol{\vartheta}) = \mathbf{B}(\mathbf{U}_i)^\top \mathbf{Q}_2 \{ \boldsymbol{\theta}_0^* + \boldsymbol{\theta}_1^* \log(I_{i,s-1}) \} + \alpha_0 Z_{i,s-1} + \sum_{j=1}^p \alpha_j A_{ij,s-r} + \sum_{k=1}^q \boldsymbol{\Phi}_k^\top (X_{ik}) \boldsymbol{\xi}_k$, and $\boldsymbol{\eta}(\boldsymbol{\vartheta}) = \{\eta_{is}\}_{i=1, s=1}^{n,t}$. In addition, let the mean vector $\boldsymbol{\mu}(\boldsymbol{\vartheta}) = \{\mu_{is}(\boldsymbol{\vartheta})\}_{i,s=1}^{n,t} = \{g^{-1}(\eta_{is}(\boldsymbol{\vartheta}))\}_{i,s=1}^{n,t}$, the variance function matrix $\mathbf{V} = \text{diag}\{V(\mu_{is})\}_{i,s=1}^{n,t}$, the diagonal matrix $\mathbf{G} = \text{diag}\{g'(\mu_{is})\}_{i,s=1}^{n,t}$ with the derivative of link function as element, and the weight matrix $\tilde{\mathbf{V}} = \text{diag}\{[V(\mu_{is})g'(\mu_{is})^2]^{-1} w_{st}, i = 1, \dots, n, s = 1, \dots, t\}$, where $w_{st} = I(t - s \geq t_0)$.

Algorithm 4.1 The Penalized Iteratively Reweighted Least Squares Algorithm.

Step 1. Initialize $\boldsymbol{\eta}^{(0)}$ and $\boldsymbol{\mu}^{(0)}$ and calculate $\tilde{\mathbf{V}}^{(0)}$ and $\tilde{\mathbf{Y}}^{(0)}$ from $g'(\mu_{is}^{(0)})$ and $V(\mu_{is}^{(0)})$, $i = 1, \dots, n$, and $s = 1, \dots, t$.

Step 2. Set step $j = 0$.

```

while  $\{\boldsymbol{\alpha}, \boldsymbol{\xi}, \boldsymbol{\theta}^*\}$  not converge do
    (i) Obtain  $\boldsymbol{\alpha}^{(j+1)}, \boldsymbol{\xi}^{(j+1)}, \boldsymbol{\theta}^{*(j+1)}$  by minimizing the (4.6) with respect to  $\boldsymbol{\vartheta}$ , and  $\boldsymbol{\eta}^{(j+1)} = \boldsymbol{\eta}(\boldsymbol{\vartheta}^{(j+1)})$ 
    and  $\boldsymbol{\mu}^{(j+1)} = \boldsymbol{\mu}(\boldsymbol{\vartheta}^{(j+1)})$ .
    (ii) Update  $\tilde{\mathbf{V}}^{(j+1)}$  and  $\tilde{\mathbf{Y}}^{(j+1)}$  with  $g'(\mu_{is}^{(j+1)})$  and  $V(\mu_{is}^{(j+1)})$ ,  $i = 1, \dots, n$ ,  $s = 1, \dots, t$ , using  $\boldsymbol{\eta}^{(j+1)}$ 
    and  $\boldsymbol{\mu}^{(j+1)}$ .
    (iii) Set  $j = j + 1$ .
end

```

In order to efficiently solve the minimization in (4.5), we design a penalized iteratively reweighted least squares (PIRLS) algorithm as described below. Suppose at the j th iteration, we have $\boldsymbol{\mu}^{(j)} = \boldsymbol{\mu}(\boldsymbol{\vartheta}^{(j)})$, $\boldsymbol{\eta}^{(j)} = \boldsymbol{\eta}(\boldsymbol{\vartheta}^{(j)})$ and $\mathbf{V}^{(j)}$. Then at $(j + 1)$ th iteration, we consider the following objective function:

$$L_P^{(j+1)} = \left\| \left\{ \mathbf{V}^{(j)} \right\}^{-1/2} \left\{ \mathbf{Y} - \boldsymbol{\mu}(\boldsymbol{\vartheta}^{(j)}) \right\} \right\|^2 + \frac{1}{2} \sum_{\ell=0}^1 \lambda_{\ell} \boldsymbol{\theta}_{\ell}^{*\top} \mathbf{Q}_2^{\top} \mathbf{P} \mathbf{Q}_2 \boldsymbol{\theta}_{\ell}^*.$$

Take the first order Taylor expansion of $\boldsymbol{\mu}(\boldsymbol{\vartheta})$ around $(\boldsymbol{\vartheta}^{(j)})$, then

$$\begin{aligned} L_P^{(j+1)} &\approx \left\| \left\{ \mathbf{V}^{(j)} \right\}^{-1/2} \left[\mathbf{Y} - \boldsymbol{\mu}^{(j)} - \left\{ \mathbf{G}^{(j)} \right\}^{-1} \mathbf{F}(\boldsymbol{\vartheta} - \boldsymbol{\vartheta}^{(j)}) \right] \right\|^2 + \frac{1}{2} \sum_{\ell=0}^1 \lambda_{\ell} \boldsymbol{\theta}_{\ell}^{*\top} \mathbf{Q}_2^{\top} \mathbf{P} \mathbf{Q}_2 \boldsymbol{\theta}_{\ell}^* \\ &= \left\| \left\{ \tilde{\mathbf{V}}^{(j)} \right\}^{1/2} \left[\tilde{\mathbf{Y}}^{(j)} - \mathbf{F}(\boldsymbol{\vartheta}) \right] \right\|^2 + \frac{1}{2} \sum_{\ell=0}^1 \lambda_{\ell} \boldsymbol{\theta}_{\ell}^{*\top} \mathbf{Q}_2^{\top} \mathbf{P} \mathbf{Q}_2 \boldsymbol{\theta}_{\ell}^*, \end{aligned} \quad (4.6)$$

where $\tilde{\mathbf{Y}}^{(j)} = (\tilde{\mathbf{Y}}_1^{(j)\top}, \dots, \tilde{\mathbf{Y}}_t^{(j)\top})^{\top}$ with $\tilde{Y}_{is}^{(j)} = g'(\mu_{is}^{(j)})(Y_{is} - \mu_{is}^{(j)}) + \eta_{is}^{(j)}$ for $s = 1, \dots, t$. The detailed procedure for the PIRLS is illustrated in Algorithm 4.1. In the numerical studies, we consider the following initial values $\mu_{is}^{(0)} = Y_{is} + 0.1$ and $\eta_{is}^{(0)} = g(\mu_{is}^{(0)})$ for $i = 1, \dots, n$ and $s = 1, \dots, t$.

Compared with the traditional nonparametric techniques, such as kernel smoothing, the proposed algorithm is much more computationally efficient. Therefore, we can easily apply our method to analyze massive spatiotemporal data sets.

4.3 Modeling the Number of Fatal and Recovered Cases

To fit the proposed STEM and make predictions for cumulative positive cases, one obstacle is the lack of direct observations for the number of active cases, I_{it} . Instead, the most commonly reported number is the count of total confirmed cases, C_{it} . Some departments of public health also release information

about fatal cases D_{it} and recovered cases R_{it} , while such kind of data tends to suffer from missingness, large error and inconsistency due to its difficulty in data collection; see the discussions in KCRA (2020).

Based on the fact that $I_{it} = C_{it} - R_{it} - D_{it}$, we attempt to modeling D_{it} and R_{it} in order to facilitate the estimation and prediction of newly confirmed cases Y_{it} based on the proposed STEM model. Let $\Delta D_{it} = D_{it} - D_{i,t-1}$ be the new fatal cases on day t . Note that patients who die on any given day were infected much earlier. Using similar notations in the STEM model (3.4), we assume that

$$\Delta D_{it} | \mathbf{X}_i, \mathbf{U}_i, I_{i,t-\delta}, \mathbf{A}_{i,t-r} \sim \text{Poisson}(\mu_{it}^D), \quad (4.7)$$

where $\delta = 14$ is the time delay between illness and death as suggested in Baud et al. (2020), and

$$\log(\mu_{it}^D) = \beta_{0t}^D(\mathbf{U}_i) + \beta_{1t}^D \log(I_{i,t-14}) + \sum_{j=1}^p \alpha_{jt}^D A_{ij,t-r} + \sum_{k=1}^q \gamma_{kt}^D (X_{ik}).$$

Ideally, if sufficient data for recovered cases can be collected from each area, a similar model can be fitted to explain the growth of the recovered cases. However, there are no uniform criteria to collect recovery reports across the U.S. (Howard and Yu, 2020). According to the CDC, severe cases with COVID-19 often require medical care and receive supportive care in the hospital. At the same time, in general, most people with the mild illness are not hospitalized and suggested to recover at home. Currently, only a few states regularly update the number of recovered patients, but seldom can the counts be mapped to counties.

Due to the lack of data, we are no longer able to use all the explanatory variables discussed above to model daily new recovered cases. Instead, we mimic the relationship between the number of recovered and active cases from some Compartmental models in epidemiology (Anastassopoulou et al., 2020; Siettos and Russo, 2013). At current time point t , we assume that $\Delta R_{is} = \nu_t I_{i,s-1} + \varepsilon_{is}$, $s = t - t_0, \dots, t$, in which the recovery rate ν_t enables us to make reasonable predictions for future recovered patients counts and provide researchers with the foresight of when the epidemic will end. The rate ν_t can be either estimated from available state-level data, or obtained from prior medical studies due to the under-reporting issue in actual data.

4.4 Zero-inflated Models at the Early Stage of the Outbreak

It is well known that in the early stage of an epidemic, the quality of any model output can be affected by the restricted quality of data that pertain to under-detection or inconsistent detection of cases, reporting delays, and poor documentation, regarding infections, deaths, tests, and other factors. There are many counties with zero daily counts at the early stage of disease spread. Therefore, we consider zero-inflated models based on a zero-inflated probability distribution, i.e., a distribution that allows for frequent zero-valued observations. Following the previous works (Arab et al., 2012; Wood et al., 2016), we

assume the observed counts Y_{it} contributes to a zero-inflated Poisson (ZIP) distribution, $\text{ZIP}(\mu_{it}^I, p_{it}^I)$, specifically, we assume that

$$P(Y_{it} = y | I_{i,t-1}, \mathbf{Z}_{i,t-1}, \mathbf{A}_{i,t-r}, \mathbf{X}_i, \mathbf{U}_i) = \begin{cases} 1 - p_{it}^I, & y = 0, \\ p_{it}^I \frac{(\mu_{it}^I)^y}{\{\exp(\mu_{it}^I) - 1\} y!}, & y > 0, \end{cases}$$

where μ_{it}^I follows (3.4), $p_{it}^I = \text{logit}(\eta_{it}^I)$ with $\eta_{it}^I = a_1 + \{b_0 + \exp(a_2)\} \log(\mu_{it}^I)$ and a_1, a_2 are unknown parameters. Here we take $b_0 = 0$ and a_1, a_2 are estimated with the roughness parameters. See Wood et al. (2016) for the estimation of a_1 and a_2 .

Let $\Delta D_{it} = D_{it} - D_{i,t-1}$ be the number of new fatal cases on day t . Similarly, we can consider zero-inflated models for fatal cases, in which we assume the observed count ΔD_{it} contributes to a ZIP distribution $\text{ZIP}(\mu_{it}^D, p_{it}^D)$:

$$P(\Delta D_{it} = d | I_{i,t-1}, \mathbf{A}_{i,t-r}, \mathbf{X}_i, \mathbf{U}_i) = \begin{cases} 1 - p_{it}^D, & d = 0, \\ p_{it}^D \frac{(\mu_{it}^D)^d}{\{\exp(\mu_{it}^D) - 1\} d!}, & d > 0, \end{cases}$$

where $p_{it}^D = \text{logit}(\eta_{it}^D)$ with $\eta_{it}^D = v_1 + \{c + \exp(v_2)\} \log(\mu_{it}^D)$, and v_1, v_2 are unknown parameters that can be similarly estimated as in the above.

5 Forecast and Band of the Forecast Path

Understanding the impact of COVID-19 requires accurate forecasting of the spread of infectious cases as well as analysis of the number of deaths and recoveries. In this section, we describe our prediction procedure of these counts; specifically, we are interested in predicting the number of new infected cases and deaths. We also provide the prediction band to quantify the uncertainty of the prediction.

5.1 The h -step Ahead Prediction

We first consider an h -step ahead prediction. If we observe $C_{is}, I_{is}, R_{is}, D_{is}$ for $s = 1, \dots, t$, then the infection model and fatal cases model can be fitted by regressing $\{Y_{is}\}_{i=1, s=t-t_0}^{n,t}$, $\{\Delta D_{is}\}_{i=1, s=t-t_0}^{n,t}$ on $\{I_{i,s-1}, Z_{i,s-1}, \mathbf{A}_{i,s-r}, \mathbf{X}_i\}_{i=1, s=1}^{n,t}$, respectively. In our forecast, we fit the infection model (3.1) and death model (3.2) alternatively to update the predicted number of cases in each compartment. To be specific, the predictions of at $t + h$ are

$$\hat{Y}_{i,t+h} = g^{-1} \left\{ \hat{\beta}_0^I(\mathbf{U}_i) + \hat{\beta}_1^I(\mathbf{U}_i) \log(\hat{I}_{i,t+h-1}) + \hat{\alpha}_0^I \hat{Z}_{i,t+h-1} + \sum_{j=1}^p \hat{\alpha}_j^I A_{ij,t+h-r} + \sum_{k=1}^q \hat{\gamma}_k^I(X_{ik}) \right\}, \quad (5.1)$$

where $\hat{I}_{i,t+h-1} = \hat{C}_{i,t+h-1} - \hat{R}_{i,t+h-1} - \hat{D}_{i,t+h-1}$, $\hat{C}_{i,t+h-1} = I_{it} + \sum_{j=t+1}^{t+h-1} \hat{Y}_{ij}$, and $\hat{Z}_{i,t+h-1} = \log(N_i - \hat{C}_{i,t+h-1}) - \log(N_i)$. Meanwhile, let

$$\widehat{\Delta D}_{i,t+h} = g^{-1} \left\{ \hat{\beta}_0^D(\mathbf{U}_i) + \hat{\beta}_1^D(\mathbf{U}_i) \log(I_{i,t+h-\delta}) + \sum_{j=1}^p \hat{\alpha}_j^D A_{ij,t+h-r'} + \sum_{k=1}^q \hat{\gamma}_k^D(X_{ik}) \right\},$$

and $\widehat{\Delta R}_{i,t+h} = \widehat{\nu}^R \widehat{I}_{i,t+h-1}$, where we predict $R_{i,t+h}$ by $\widehat{R}_{i,t+h} = R_{it} + \sum_{s=1}^h \widehat{\Delta R}_{i,t+s}$, and $D_{i,t+h}$ by $\widehat{D}_{i,t+h} = D_{it} + \sum_{s=1}^h \widehat{\Delta D}_{i,t+s}$. Then, the predicted number of active cases and susceptible cases are $\widehat{I}_{i,t+h} = \widehat{C}_{i,t+h-1} + \widehat{Y}_{i,t+h} - \widehat{R}_{i,t+h} - \widehat{D}_{i,t+h}$, and $\widehat{S}_{i,t+h} = N_i - (\widehat{C}_{i,t+h-1} + \widehat{Y}_{i,t+h})$. The above one-step predicted values can be plugged back into equation (5.1) to obtain the predictions for the following days by repeating the same procedure.

5.2 Prediction Bands

There is substantial interest in quantifying the uncertainty for the forecasts with a succession of periods; see, for example, Kong et al. (2018) and Murray et al. (2020). To assess the uncertainty associated with the prediction, we propose to develop a prediction band that provides an upper and lower expectation for the real path of the observations.

To construct the band for forecast path $\{Y_{i,t+h}, h = 1, \dots, H\}$, we consider the bootstrap method (Staszewska-Bystrova, 2009), in which the bootstrap samples are generated using the bias-corrected bootstrap procedure. Bootstrapping is a powerful and flexible data analysis tool, which allows us to assign measures of accuracy. By simulating the observed data from our estimated model, we collect the bootstrap samples. For a given bootstrap sample, we re-estimate the model, and produce the corresponding forecast paths. The prediction uncertainty comes from two parts: the estimation variation and the variation from the individual bootstrap sample. We construct $100(1 - \alpha)\%$ prediction band based on the envelope covering all the forecast paths after deleting $100\alpha\%$ extreme paths from all bootstrap paths. See Algorithms 5.1 and 5.2 for the details.

6 A Simulation Study

In this section, we conduct a simulation study to evaluate the finite sample performance of the proposed method. In the simulation, we use a subset of covariates of the county-level characteristics analyzed in Section 7. The response variable Y_{it} and ΔD_{it} are generated from a ZIP distribution with the logarithm of Poisson parameters generated as following:

$$\log(\mu_{it}^I) = \beta_0^I(\mathbf{U}_i) + \beta_1^I(\mathbf{U}_i) \log(I_{i,t-1}) + \sum_{j=1}^p \alpha_j^I A_{ij,t-r} + \sum_{k=1}^q \gamma_k^I(X_{ik}), \quad (6.1)$$

$$\log(\mu_{it}^D) = \beta_0^D(\mathbf{U}_i) + \beta_1^D \log(I_{i,t-\delta}), \quad (6.2)$$

where $\delta = 14$, $p = 2$, $q = 5$, $r = 7$, and A_{ijt} , X_{ik} , $j = 1, 2$, $k = 1, \dots, 5$, come from the covariates in the COVID-19 dataset described in Section 2. The true univariate functions $\gamma_1(x)$, $\gamma_2(x)$, \dots , $\gamma_5(x)$, together with their estimate and confidence bands in one typical iteration, are displayed in Figure 6.1 (a)–(e). Figure 6.2 (a)–(c) depict the bivariate coefficient functions $\beta_0^I(\cdot)$, $\beta_1^I(\cdot)$ and $\beta_0^D(\cdot)$, which are generated to mimic the spatial pattern of infection/mortality rate in the pandemic. We

Algorithm 5.1 A bootstrap procedure to correct the bias.

Step 1. Fit models (3.1) and (3.2) using $(Y_{is}, I_{i,s-1}, Z_{i,s-1}, \mathbf{A}_{i,s-r}, \mathbf{X}_i, \mathbf{U}_i)_{i=1,s=1}^{n,t}$ and $(\Delta D_{is}, I_{i,s-1}, \mathbf{A}_{i,s-r}, \mathbf{X}_i, \mathbf{U}_i)_{i=1,s=1}^n$, obtain $\hat{\beta}^I, \hat{\alpha}^I, \hat{\gamma}^I, \hat{\beta}^D, \hat{\alpha}^D, \hat{\gamma}^D, \hat{\nu}^R, \hat{a}$, and \hat{v} .

Step 2. Generate bootstrap samples to correct the bias in the estimator of the coefficients.

foreach $1 \leq b \leq B$ **do**

(i) Generate the bootstrap sample as follows.

foreach $1 \leq s \leq t$ **do**

Generate $Y_{is}^b \sim \text{ZIP}(\hat{\mu}_{is}^I, \hat{p}_{is}^I)$, $\Delta D_{is}^b \sim \text{ZIP}(\hat{\mu}_{is}^D, \hat{p}_{is}^D)$, and $\Delta R_{is}^b = \hat{\nu}^R I_{i,s-\delta'}$, where

$$\hat{\mu}_{is}^I = \exp \left\{ \hat{\beta}_0^I(\mathbf{U}_i) + \hat{\beta}_1^I(\mathbf{U}_i) \log(I_{i,s-1}) + \hat{\alpha}_0^I Z_{i,s-1} + \sum_{j=1}^p \hat{\alpha}_j^I A_{ij,s-r} + \sum_{k=1}^q \hat{\gamma}_k^I(X_{ik}) \right\},$$

$$\hat{\mu}_{is}^D = \exp \left\{ \hat{\beta}_0^D(\mathbf{U}_i) + \hat{\beta}_1^D(\mathbf{U}_i) \log(I_{i,s-\delta}) + \sum_{j=1}^p \hat{\alpha}_j^D A_{ij,s-r'} + \sum_{k=1}^q \hat{\gamma}_k^D(X_{ik}) \right\},$$

$$\hat{p}_{is}^I = \text{logit} \left[\hat{a}_1 + \{b_0 + \exp(\hat{a}_2)\} \log(\hat{\mu}_{is}^I) \right], \quad \hat{p}_{is}^D = \text{logit} \left[\hat{v}_1 + \{b_0 + \exp(\hat{v}_2)\} \log(\hat{\mu}_{is}^D) \right].$$

Update $Z_{is}^b = \log(S_{is}^b/N_i)$, where $S_{is}^b = S_{i,s-1}^b - Y_{is}^b$ and $I_{is}^b = I_{i,s-1} + Y_{is}^b - \Delta D_{is}^b - \Delta R_{is}^b$.

end

(ii) Fit the models (3.1) and (3.2) based on $(Y_{is}^b, I_{i,s-1}^b, Z_{i,s-1}, \mathbf{A}_{i,s-r}, \mathbf{X}_i, \mathbf{U}_i)_{i=1,s=1}^{n,t}$ and $(\Delta D_{is}^b, I_{i,s-\delta}^b, \mathbf{A}_{i,s-r'}, \mathbf{X}_i, \mathbf{U}_i)_{i=1,s=1}^{n,t}$, respectively, and obtain $(\hat{\beta}^{I,b}, \hat{\alpha}^{I,b}, \hat{\gamma}^{I,b}, \hat{a}^b)$ and $(\hat{\beta}^{D,b}, \hat{\alpha}^{D,b}, \hat{\gamma}^{D,b}, \hat{v}^b)$.

end

Step 3. Calculate the bias of the coefficients based on the above bootstrap samples. For example, for $\ell = 0, 1$, let $\text{bias}(\hat{\beta}_\ell^I) = B^{-1} \sum_{b=1}^B \hat{\beta}_\ell^{I,b} - \hat{\beta}_\ell^I$, and let $\hat{\beta}_\ell^{I,c} = \hat{\beta}_\ell^I - \text{bias}(\hat{\beta}_\ell^I)$ be the corrected coefficient function. Similarly, we obtain the bias-corrected coefficients of $\hat{\alpha}_t, \hat{\gamma}_t, \hat{a}$, and \hat{v} , denoted by $\hat{\alpha}_t^c, \hat{\gamma}_t^c, \hat{a}^c$, and \hat{v}^c , respectively.

Algorithm 5.2 A bootstrap procedure to calculate the prediction band.

Step 1. Generate bootstrap samples to construct prediction band.

foreach $1 \leq b \leq B$ **do**

foreach $1 \leq h \leq H$ **do**

 Generate $Y_{i,t+h}^b \sim \text{ZIP}(\hat{\mu}_{i,t+h}^{I,c,b}, \hat{p}_{i,t+h}^{I,c,b})$, $\Delta D_{i,t+h}^b \sim \text{ZIP}(\hat{\mu}_{i,t+h}^{D,c,b}, \hat{p}_{i,t+h}^{D,c,b})$, and $\Delta R_{i,t+h}^b = \hat{\nu}^R I_{i,t+h-\delta'}$ based on bootstrap estimators, where

$$\hat{\beta}^{I,c,b} = 2\hat{\beta}^I - \hat{\beta}^{I,b}, \hat{\alpha}^{I,c,b} = 2\hat{\alpha}^I - \hat{\alpha}^{I,b}, \hat{\gamma}^{I,c,b} = 2\hat{\gamma}^I - \hat{\gamma}^{I,b}, \hat{a}^{c,b} = 2\hat{a} - \hat{a}^b$$

$$\hat{\beta}^{D,c,b} = 2\hat{\beta}^D - \hat{\beta}^{D,b}, \hat{\alpha}^{D,c,b} = 2\hat{\alpha}^D - \hat{\alpha}^{D,b}, \hat{\gamma}^{D,c,b} = 2\hat{\gamma}^D - \hat{\gamma}^{D,b}, \hat{v}^{c,b} = 2\hat{v} - \hat{v}^b,$$

$$\hat{\mu}_{i,t+h}^{I,c,b} = \exp \left\{ \hat{\beta}_0^{I,c,b}(\mathbf{U}_i) + \hat{\beta}_1^{I,c,b}(\mathbf{U}_i) \log(I_{i,t+h-1}) + \hat{\alpha}_0^{I,c,b} Z_{i,t+h-1} \right. \\ \left. + \sum_{j=1}^q \hat{\alpha}_j^{I,c,b} A_{ij,t+h-r} + \sum_{k=1}^q \hat{\gamma}_k^{I,c,b}(X_{ik}) \right\},$$

$$\hat{\mu}_{i,t+h}^{D,c,b} = \exp \left\{ \hat{\beta}_0^{D,c,b}(\mathbf{U}_i) + \hat{\beta}_1^{D,c,b} \log(I_{i,t+h-\delta}) + \sum_{j=1}^p \hat{\alpha}_j^{D,c,b} A_{ij,t+h-r'} + \sum_{k=1}^q \hat{\gamma}_k^{D,c,b}(X_{ik}) \right\},$$

$$\hat{p}_{i,t+h}^{I,c,b} = \text{logit} \left[\hat{a}_1^{c,b} + \{b_0 + \exp(\hat{a}_2^{c,b})\} \log(\hat{\mu}_{i,t+h}^{I,c,b}) \right],$$

$$\hat{p}_{i,t+h}^{D,c,b} = \text{logit} \left[\hat{v}_1^{c,b} + \{b_0 + \exp(\hat{v}_2^{c,b})\} \log(\hat{\mu}_{i,t+h}^{D,c,b}) \right].$$

 Update $Z_{i,t+h}^b = \log(S_{i,t+h}^b/N_i)$, where $S_{i,t+h}^b = S_{i,t+h-1}^b - Y_{i,t+h}^b$ and $I_{i,t+h}^b = I_{i,t+h-1}^b + Y_{i,t+h}^b - \Delta D_{i,t+h}^b - \Delta R_{i,t+h}^b$.

end

end

Step 2. Construct the $100(1 - \alpha)\%$ prediction band by the above B bootstrap paths with the most extreme αB paths discarded. Start with setting $\kappa = 0$.

while $\kappa < \alpha B$ **do**

 (i) For each forecast time point $h = 1, \dots, H$ (there are in total $B - \kappa$ constructed paths available), identify the largest and the smallest bootstrap forecast values, and the associated paths. Notice there are $2H$ extreme values and at most corresponding $2H$ paths.

 (ii) Compute the distances from each of the bootstrap path (at most $2H$) to the bootstrap sample, based on: $\sum_{h=1}^H (\hat{\mu}_{i,t+h}^c - Y_{i,t+h}^b)^2$ or $\sum_{h=1}^H |\hat{\mu}_{i,t+h}^c - Y_{i,t+h}^b|$.

 (iii) Remove the path with the largest distance, and set $\kappa = \kappa + 1$.

end

Step 3. Obtain the $100(1 - \alpha)\%$ prediction band from the envelope of the remaining $(1 - \alpha)B$ paths.

also include the corresponding estimated functions from one experiment in Figure 6.2 (d)–(f) to show that the spatial pattern can be very well captured using the proposed method. For recovery data, the daily recovered cases are simulated by $\Delta R_{it} = \nu^R I_{i,s-1}$, where $\nu^R = 0.07$. We simulate data by assuming that a pandemic emerged on March 15 with 1 case showed up in each of the 420 selected counties. These counties are selected if COVID-19 cases had been found by March 15 in real data. Then, daily confirmed, fatal and recovered cases are generated based on model (6.1) and (6.2) from a ZIP distribution with the complimentary log of the zero probability being linearly dependent on the log of the Poisson parameter μ_{it}^I and μ_{it}^D .

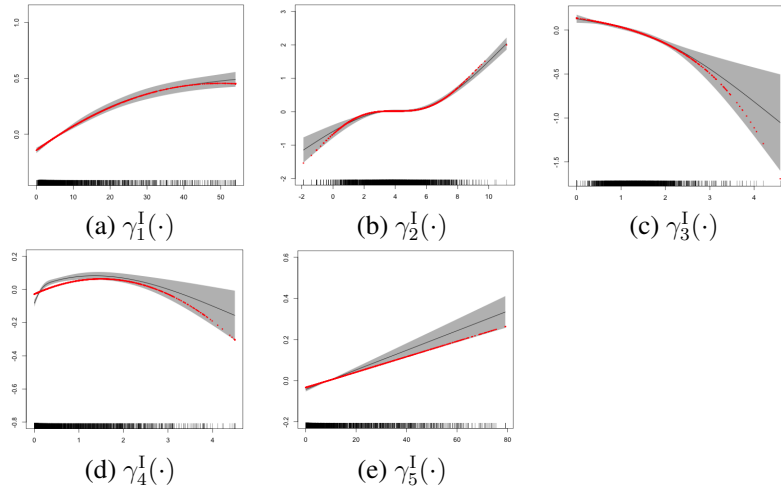


Figure 6.1: The true and estimated univariate component functions in model (6.1) (estimation window: 04/17/20–04/30/20). The red curves represent true functions, while black curves and dark area indicate estimated coefficients and their 95% confidence bands.

To evaluate the performance numerically, we conduct 100 Monte Carlo experiments with 9 or 14 days as the training window sizes. For the univariate spline smoothing, we use cubic splines with two interior knots; and for the bivariate spline smoothing, we consider degree $d = 2$, smoothness $r = 1$, and two different triangulations in Figure 6.3: \triangle_1 (119 triangles with 87 vertices) and \triangle_2 (522 triangles with 306 vertices). The root mean squared error (RMSE) for the parametric and nonparametric components in models (6.1) and (6.2) are reported in Table 6.1. According to the numeric results, the proposed model is not sensitive to the choice of triangulation. However, increasing the window size of training data can help improve the accuracy in estimating most of the coefficient functions.

In addition, the root mean squared prediction error for h -day ahead predictions using 14 days as the training period are presented in Table 6.2, $h = 1, \dots, 28$. For comparison, we also consider the naive model that assumes a linear growth pattern for total confirmed cases for each county that

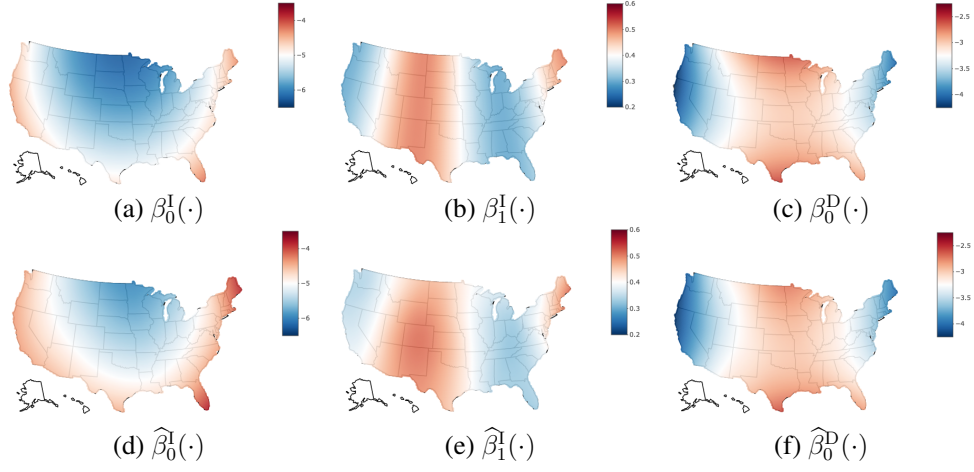


Figure 6.2: True and estimated bivariate varying coefficients (estimation window: 04/17/20-04/30/20) in the simulation.

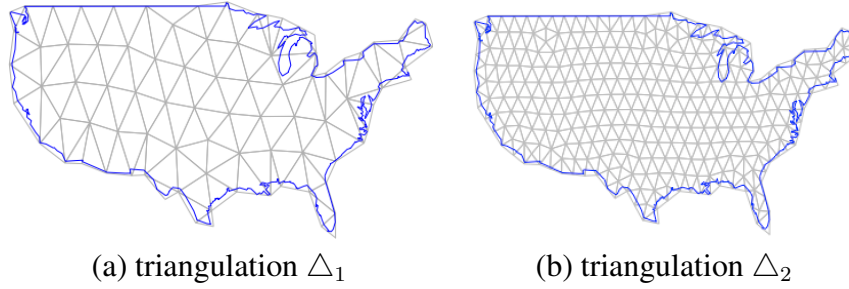


Figure 6.3: Triangulations used in the bivariate spline estimation.

Table 6.1: The average of root mean squared errors (RMSEs) of the estimated components in infection model and death model in the simulation (“—” indicates not applicable).

Model	Window	Component								
	Size	β_0	β_1	α_1	α_2	γ_1	γ_2	γ_3	γ_4	γ_5
Infection	9 days	0.5094	0.0453	0.0534	0.0258	0.0105	0.0415	0.0214	0.0262	0.0114
	14 days	0.4862	0.0395	0.0499	0.0193	0.0103	0.0416	0.0186	0.0256	0.0119
Death	9 days	0.0456	0.0999	—	—	—	—	—	—	—
	14 days	0.0373	0.1000	—	—	—	—	—	—	—

$E(C_{it}|t) = \beta_{i0} + \beta_{i1}t$, $\text{Var}(C_{it}|t) = \sigma_i^2$, where C_{it} stands for the number of total confirmed cases in i th county. Comparing with the linear model separately fitted for each county without taking into account the spatial correlation, the prediction performance of STEM is better, especially for the long-term forecast. We further construct 95% prediction bands based on the proposed bootstrap method and calculate the empirical coverage rate based on 100 replications. Table 6.3 reports summary statistics of the coverage rates for 3104 counties in 48 contiguous states. For each county, we examine how often, out of 100 iterations, that the true infected/fatal cases curve falls inside the band all the time for a two-week or four-week forecasting period. Eventually, the coverage rates are very close to the nominal level for most counties, as shown by the quartiles.

Table 6.2: The average of root mean squared prediction errors (RMSPE) of the infection or death count, where D_h is for the h -day ahead prediction, $h = 1, \dots, 28$.

Infection Model										
Model	D ₁	D ₂	D ₃	D ₄	D ₅	D ₆	D ₇	D ₈	D ₉	D ₁₀
STEM	3.28	5.01	6.76	8.36	9.93	11.55	13.58	15.32	17.15	18.94
Linear	7.11	9.53	11.99	14.57	17.76	21.10	24.88	29.24	34.08	39.58
Model	D ₁₁	D ₁₂	D ₁₃	D ₁₄	D ₁₅	D ₁₆	D ₁₇	D ₁₈	D ₁₉	D ₂₀
STEM	20.91	22.83	24.78	26.68	28.76	30.86	32.93	35.20	37.34	39.54
Linear	45.71	52.23	58.98	66.09	73.27	80.55	88.03	95.72	103.75	112.25
Model	D ₂₁	D ₂₂	D ₂₃	D ₂₄	D ₂₅	D ₂₆	D ₂₇	D ₂₈		
STEM	41.77	43.94	46.17	48.47	52.68	55.42	58.27	61.22		
Linear	121.27	130.83	140.92	151.77	166.06	181.3	197.78	215.55		
Death Model										
Model	D ₁	D ₂	D ₃	D ₄	D ₅	D ₆	D ₇	D ₈	D ₉	D ₁₀
STEM	1.17	1.67	2.05	2.40	2.7	2.96	3.21	3.45	3.68	3.90
Linear	2.43	3.16	3.91	4.67	5.47	6.31	7.20	8.13	9.10	10.08
Model	D ₁₁	D ₁₂	D ₁₃	D ₁₄	D ₁₅	D ₁₆	D ₁₇	D ₁₈	D ₁₉	D ₂₀
STEM	4.08	4.29	4.49	4.69	4.87	5.04	5.18	5.33	5.47	5.60
Linear	11.06	12.11	13.21	14.32	15.46	16.66	17.84	19.11	20.39	21.69
Model	D ₂₁	D ₂₂	D ₂₃	D ₂₄	D ₂₅	D ₂₆	D ₂₇	D ₂₈		
STEM	5.78	5.93	6.10	6.26	6.42	6.59	6.76	6.95		
Linear	23.02	24.38	25.81	27.26	28.78	30.3	31.89	33.53		

7 Analysis and Findings in COVID-19

The goals of the following study are two-fold. First, we develop a new dynamic epidemic modeling framework for public health surveillance data to study the spatiotemporal pattern in the spread of

Table 6.3: The empirical coverage rate of the 95% projection band.

Infection Model			Death Model		
Quantile	Number of prediction days		Quantile	Number of prediction days	
	14 days	28 days		14 days	28 days
Q1	95%	90%	Q1	96%	93%
Q2	97%	93%	Q2	97%	95%
Q3	98%	95%	Q3	98%	96%

COVID-19. We aim to investigate whether the proposed model could guide the modeling of the dynamics of the spread at the county level by moving beyond the typical theoretical conceptualization of context where a county’s infection is only associated with its own features. Second, to understand the factors that contribute to the spread of COVID-19, we model the daily infected cases at the county level, considering the demographic, environmental, behavioral, and socioeconomic factors in the U.S.

7.1 Estimation and Inference for the STEM

For the model estimation, we consider the following model for the infected count:

$$\begin{aligned}
\log(\mu_{it}^I) = & \beta_{0t}^I(\mathbf{U}_i) + \beta_{1t}^I(\mathbf{U}_i) \log(I_{i,t-1}) + \alpha_{0t}^I Z_{i,t-1} + \alpha_{1t}^I \text{Control}_{i,t-7} + \alpha_{2t}^I \text{Mobility}_{i,t-7} \\
& + \gamma_{1t}^I(\text{Gini}_i) + \gamma_{2t}^I(\text{Affluence}_i) + \gamma_{3t}^I(\text{Disadvantage}_i) + \gamma_{4t}^I(\text{Urban}_i) + \gamma_{5t}^I(\text{PD}_i) \\
& + \gamma_{6t}^I(\text{Tbed}_i) + \gamma_{7t}^I(\text{NHIC}_i) + \gamma_{8t}^I(\text{EHPC}_i) \\
& + \gamma_{9t}^I(\text{AA}_i) + \gamma_{10t}^I(\text{HL}_i) + \gamma_{11t}^I(\text{Sex}_i) + \gamma_{12t}^I(\text{Old}_i),
\end{aligned} \tag{7.1}$$

where $i = 1, \dots, 3104$. For the death count, we consider the following semiparametric model:

$$\begin{aligned}
\log(\mu_{it}^D) = & \beta_{0t}^D(\mathbf{U}_i) + \beta_{1t}^D \log(I_{i,t-\delta}) + \alpha_{1t}^D \text{Control}_{i,t-7} + \alpha_{2t}^D \text{Mobility}_{i,t-7} \\
& + \gamma_{1t}^D \text{Gini}_i + \gamma_{2t}^D \text{Affluence}_i + \gamma_{3t}^D \text{Disadvantage}_i + \gamma_{4t}^D \text{Urban}_i + \gamma_{5t}^D \text{PD}_i \\
& + \gamma_{6t}^D \text{Tbed}_i + \gamma_{7t}^D \text{NHIC}_i + \gamma_{8t}^D \text{EHPC}_i + \gamma_{9t}^D \text{AA}_i + \gamma_{10t}^D \text{HL}_i + \gamma_{11t}^D \text{Sex}_i + \gamma_{12t}^D \text{Old}_i.
\end{aligned} \tag{7.2}$$

We consider the data collected from March 16 to September 3, 2020; see the data description in Section 2. Note that in models (7.1) and (7.2), the covariate Control_{it} is a dummy variable for the executive order “shelter-in-place” or “stay-at-home”, namely $\text{Control}_{it} = 1$ suggesting “shelter-in-place” taken place for county i at time t , while $\text{Control}_{it} = 0$ suggesting no restriction or restriction lifted. See Table 2.1 for details of other county-level predictors.

We use 28 days, two incubation periods, as an estimation window to examine how the covariates affect the newly infected cases and fatal cases, and we choose $\delta = 14$. The roughness parameters are selected by the generalized cross-validation (GCV). The performance of the univariate and bivariate splines is dependent upon the choice of the knots and triangulations, respectively. We use cubic splines

with two interior knots for the univariate spline smoothing. We generate the triangulations according to “max-min” criterion, which maximizes the minimum angle of all the angles of the triangles in the triangulation. We consider the same triangulations as shown in Figure 6.3: \triangle_1 and \triangle_2 . By the “max-min” criterion, \triangle_2 is better than \triangle_1 , but it also significantly increases the number of parameters to estimate. As a trade-off, for the estimation of $\beta_0^I(\cdot)$ and $\beta_1^I(\cdot)$, we adopt the finer triangulation \triangle_2 , and use the rough triangulation \triangle_1 to estimate $\beta_0^D(\cdot)$ due to the sparsity problem in the death count and many zeros observed.

First of all, we describe our findings from modeling the COVID-19 related infection counts in 3,104 counties from the 48 mainland US states and the District of Columbia. To examine the effect of the control measures (“shelter-in-place” or “stay-at-home” orders) and mobility level after 7 days, we test the hypothesis: $H_0 : \alpha_{jt}^I = 0$, $j = 1, 2$ in model (7.1). Figure 7.1 (a) shows that the control measure is significant for the infected count most of the time. Figure 7.1 (b) shows that the p -value of the mobility is always less than 0.0001, and thus the mobility is significant for the entire study period.

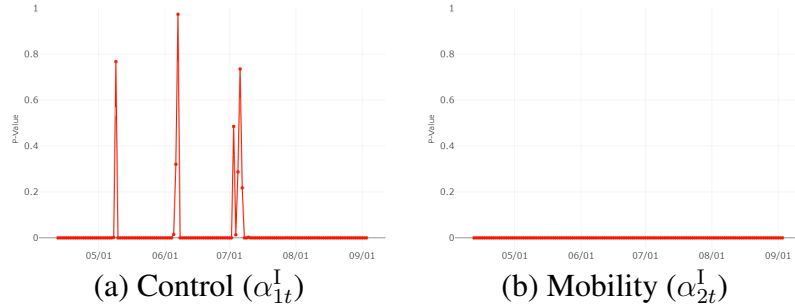


Figure 7.1: P-values of hypothesis tests of constant coefficients in model (7.1).

Next, we examine the effect of the other predictors in Model (7.1). To test hypotheses $H_0 : \gamma_{kt}^I(\cdot) = 0$, $k = 1, \dots, 12$, we construct the 95% simultaneous confidence band (SCB) for $\gamma_{kt}^I(\cdot)$'s. In function estimation problems, SCBs are an important tool to quantify and visualize the variability of the functional components; see Wang and Yang (2009), Cao et al. (2012), and Zheng et al. (2016) for some related theory and applications. We consider the period from 03/22/2020 to 04/18/2020 as an illustration and plot the estimated curves for different explanatory variables together with the corresponding SCBs in Figure 7.2. Based on Figure 7.2, we can observe that at the beginning of the pandemic, the infected cases increase with the population density (PD), which is consistent with our intuition. We also find that the infections increase with African American Ratio and Hispanic Latino Ratio at the beginning of the outbreak.

We also study the effect of the covariates over time. Figure 7.3 shows the effect of the aged people rate at different time points over the outbreak. In the early stage of the COVID-19 pandemic,

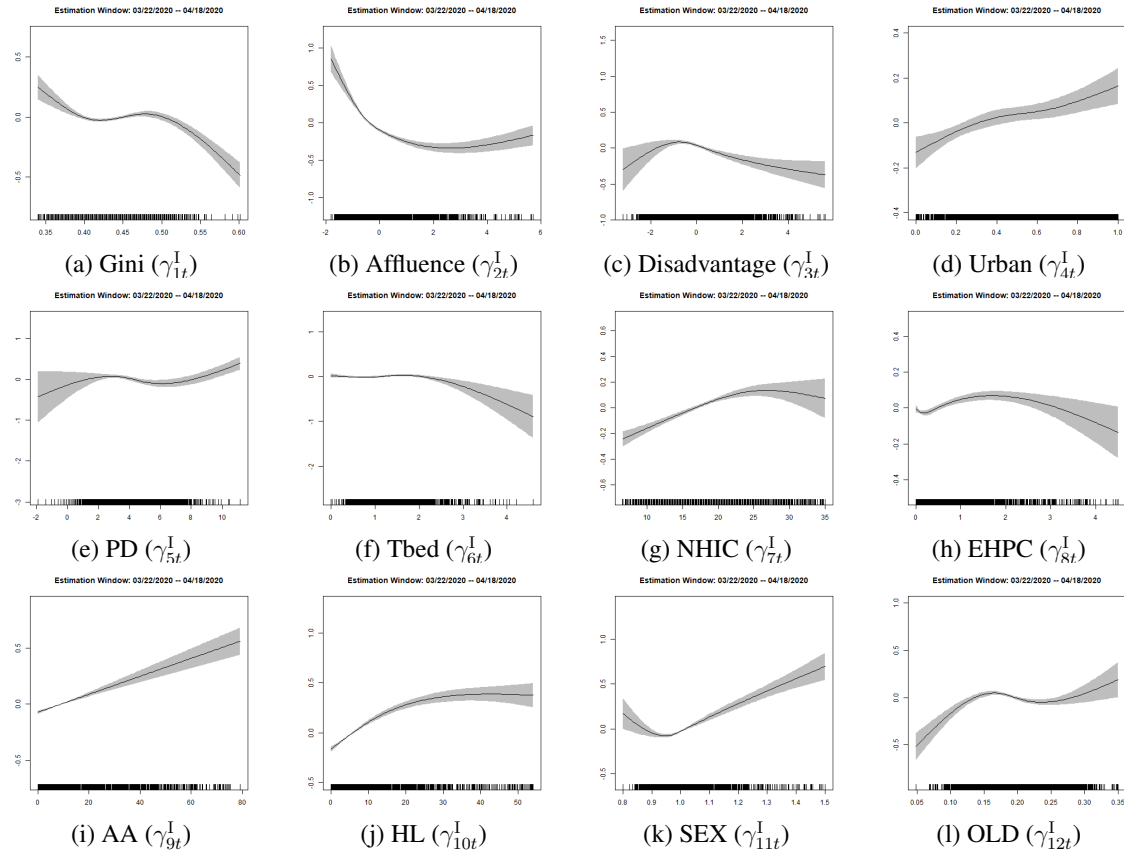


Figure 7.2: The estimated univariate functional components and the corresponding simultaneous confidence bands in the infection model.

from March to April, COVID-19 struck the elderly more severely than the younger people. By mid-April and May, we saw that those communities with less aged people suffered more from COVID-19. Counties with a very high rate of aged people still experience high infection rates. However, when people understood the virus more and took action to protect the senior people, from mid-June to September, those counties with a higher rate of aged people became those least infected.

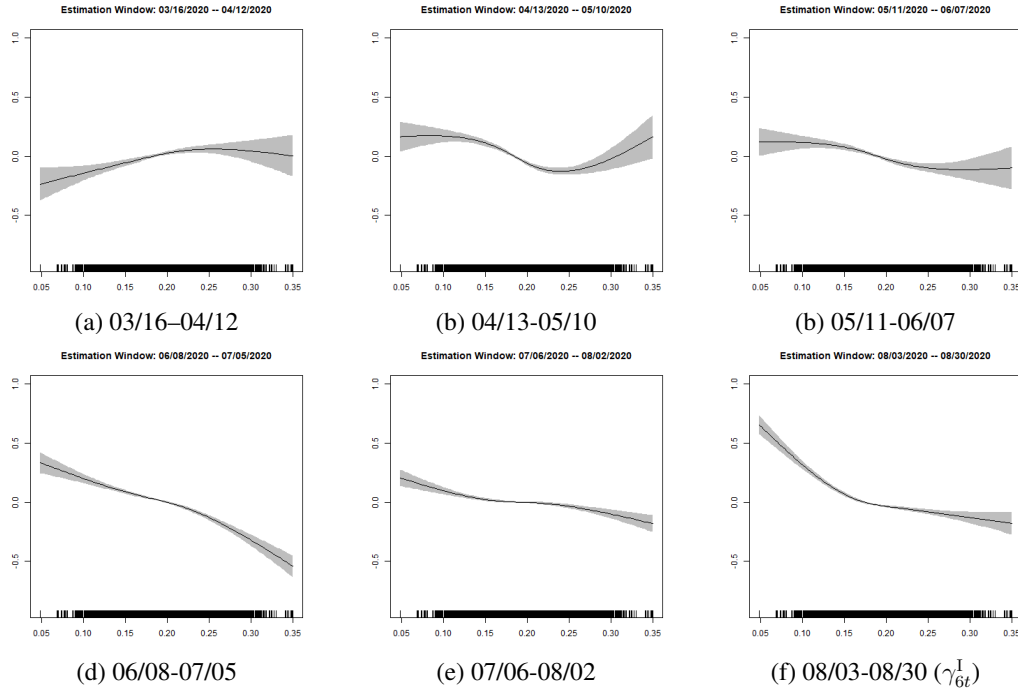


Figure 7.3: The estimated univariate functional components corresponding to the proportion of the elderly during different periods.

Movies 1-12 in the Supplementary Material show the estimates and SCBs of the nonparametric functions $\gamma_{kt}^I(\cdot)$, $k = 1, \dots, 12$, over the entire study period in the STEM model (7.1).

After the discussion of our finding in the infection model, let us focus on the death model. For Model (7.2), we focus on the following hypothesis tests: $H_0 : \alpha_{jt}^D = 0$, $j = 1, 2$, $H_0 : \beta_{1t}^D = 0$ and $H_0 : \gamma_{kt}^D = 0$, $k = 1, \dots, 12$. Figure 7.4 (b) shows that “Mobility” is significant over the entire study period. “OLD” is significant in the beginning of the pandemic. For other county-level covariates, “Affluence”, “Disadvantage”, “EHPC”, “AA” and “SEX” are significant with p -values smaller than 0.05 most of time, while the rest of the predictors are significant on some days, but insignificant on other days.

In addition, movies 13 and 14 in the Supplementary Material illustrate the estimated coefficient

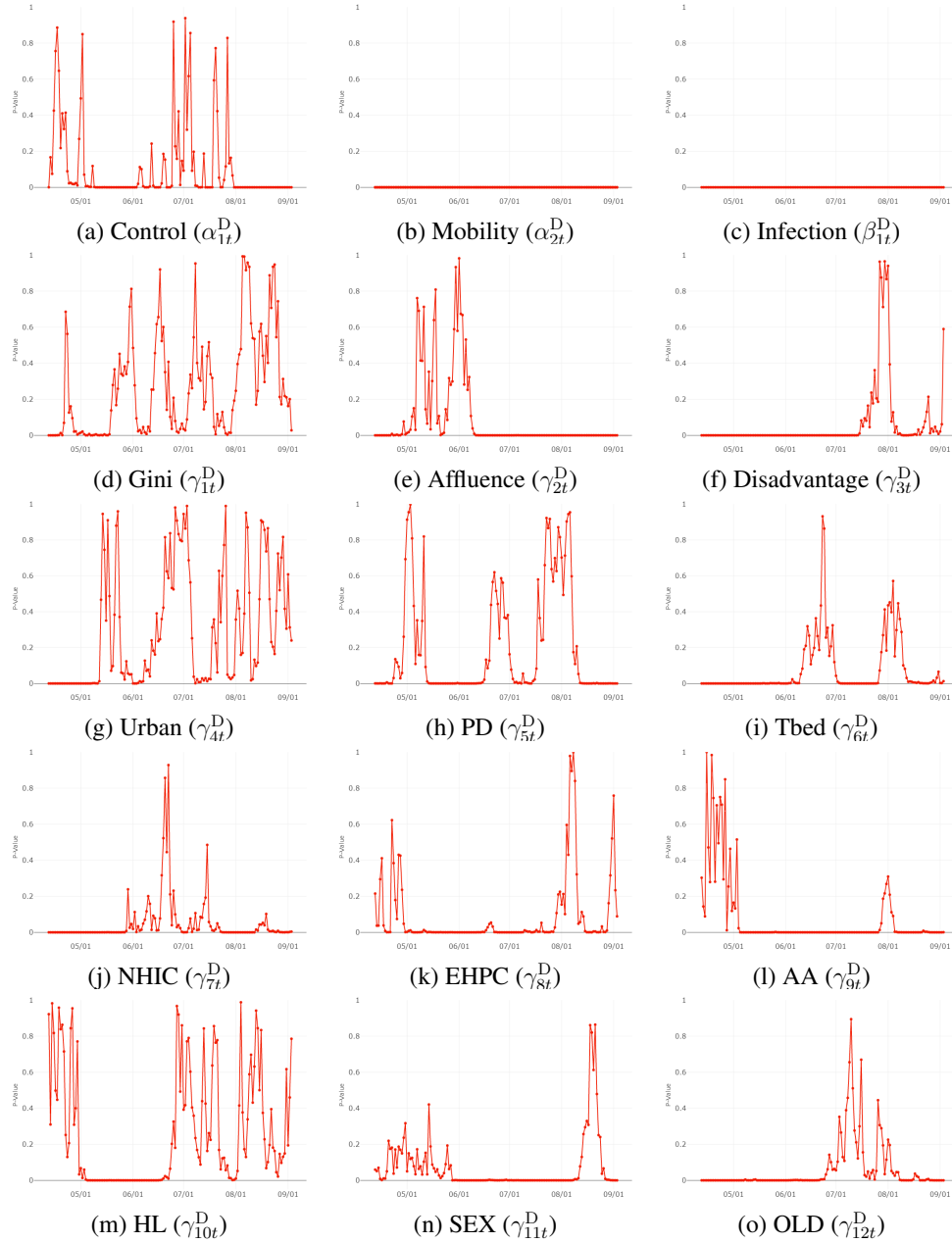


Figure 7.4: P-values of the hypothesis test of the constant coefficient in model (7.2).

functions of $\beta_0^I(\cdot)$ and $\beta_1^I(\cdot)$ in model (7.1). From Movie 13, we can see that the transmission rate, $\beta_0^I(\cdot)$, varies at different locations and in different phases of the outbreak, especially the high rate in late March and April. Movie 14 shows that $\beta_1^I(\cdot)$ also varies from one location to another location, which indicates that the homogeneous mixing assumption of the simple SIR models does not hold. The transmission rate is high in most states at the end of April; however, it became much lower since June. Movie 15 on the Supplementary Material shows the pattern of $\widehat{\beta}_{0t}^D$ in model (7.2). From this animation, we observe a severe fatality condition in the southern states in July and a pattern of general decrease in the entire U.S. since August 2020.

7.2 Short-term Forecasting Performance and Results

In this section, we investigate the short-term prediction performance of the proposed method. In the following, we consider h -day ahead prediction based on the forecasting method described in Section 5. We choose nine days as a training window for model fit to predict the next seven days, which minimizes the mean squared prediction errors.

An R shiny app (Wang et al., 2020a) is developed to provide a 7-day forecast of COVID-19 infection and death count at both the county level and state level, in which the state level forecast is obtained by aggregating forecasts across counties in each state. This app was launched on 03/27/2020 for displaying the results of our 7-day forecasting.

We demonstrate the accuracy of the STEM for h -day ahead predictions, $h = 1, \dots, 7$. For comparison, we also consider the two naive models that assume a linear or exponential growth pattern for total confirmed cases for each county: for $i = 1, \dots, n$,

- (Linear) $E(C_{it}|t) = \beta_{i0} + \beta_{i1}t$, $\text{Var}(C_{it}|t) = \sigma_i^2$;
- (Exponential, Poisson) $\log\{E(C_{it}|t)\} = \beta_{i0} + \beta_{i1}t$, $\text{Var}(C_{it}|t) = \exp(\beta_{i0} + \beta_{i1}t)$;

and the following simple epidemic method (EM):

- (EM) $\log(\mu_{it}) = \beta_0 + \beta_1 \log(I_{i,t-1})$, $\log(\mu_{it}^D) = \beta_0^D + \beta_1^D \log(I_{i,t-14})$.

We consider the data collected from April 8 to September 3, 2020. To show the accuracy of different methods, we compute the following root mean-squared prediction errors (RMSPEs):

$$R_h = T^{-1} \sum_{t=1}^T \left\{ n^{-1} \sum_{i=1}^n (\widehat{Y}_{i,t+h} - Y_{i,t+h})^2 \right\}^{1/2}, \quad h = 1, \dots, 7,$$

where $T = 119$.

Table 7.1 shows the average of the RMSPEs for h -day. From this table, we can see that our proposed method performs the best in predicting the infection count regardless of the date for prediction.

When predicting the death count, both EM and STEM methods outperform the other competitors. Overall, we can see that our proposed method outperforms other competing methods in terms of the prediction accuracy. When we analyze the COVID-19 dataset, we also notice a strong temporal-pattern. To be more specific, at the beginning of this pandemic, a more complex model is necessary to describe the outbreak's different severe levels. As the pandemic expands, a simpler model can be used for future prediction. Start from middle July, a more complex model is necessary due to the pandemic's pattern change. Hence, a more flexible model like the STEM is more appropriate for COVID-19 data analysis.

Table 7.1: The average of root mean squared prediction errors (RMSPE) of the infection or death count in the COVID-19 Study, where D_h is for the h -day ahead prediction, $h = 1, \dots, 7$.

	Method	D_1	D_2	D_3	D_4	D_5	D_6	D_7
Infection	Linear	43.844	59.856	76.105	93.301	111.996	132.654	155.276
	Exponential	>1000	>1000	>1000	>1000	>1000	>1000	>1000
	EM	44.270	81.509	119.204	158.006	197.847	239.207	282.382
	STEM	35.547	53.683	72.200	91.564	111.312	131.843	154.569
Death	Linear	2.066	2.759	3.418	4.088	4.807	5.563	6.336
	Exponential	>1000	>1000	>1000	>1000	>1000	>1000	>1000
	EM	1.764	3.053	4.332	5.633	6.972	8.351	9.803
	STEM	1.411	2.203	2.927	3.615	4.283	4.932	5.629

7.3 Long-term Forecasting Performance and Results

With the rapid spread of the COVID-19 across the U.S., there has been an increasing public health concern regarding the adequacy of resources to treat infected cases. It is well known that hospital beds, intensive care units, and ventilators are critical for the treatment of patients with severe illness. To predict the timing of the outbreak peak and the number of health resources required at a peak, in this section, we also provide the long-term projection of the death counts, assuming that the future will continue to follow the current pattern, and current interventions will remain the same till the end of forecasting period.

The long-term projections are conducted at the county and state levels, respectively. Due to the lack of reliable recovered data, we consider the recovery rate uniformly distributed from $5\% \sim 15\%$, where the recovery rate is defined as the number of daily recovered cases divided by the number of active cases 14 days (one incubation period) ago. Figure 7.5 shows the one month-ahead prediction and the corresponding 95% prediction band both at the county and state level in the state of Iowa and Story County, Iowa. Table 7.2 summarizes the performance of one month-ahead projection for county-level

fatal cases. We use the root of mean squared prediction error to measure the prediction performance. Table 7.2 shows our proposed method has good prediction performance. The prediction error increases as time goes by, as the error will accumulate over time. Also, we evaluate the performance of prediction band. We calculate the empirical coverage rate: the proportion of counties for which the h -day ahead prediction band, $h = 1, \dots, 30$, covers the observed counts. From Table 7.2, we see that the empirical coverage rates of the county-level band are close to the nominal level for one week-ahead prediction, and we still have a good coverage rate even for one month-ahead prediction. The projection for other counties and states can be found from our weekly updated Shiny App (Wang et al., 2020b) and the webpage of CDC (CDC, 2020a). Note that CDC (2020a) presents predicted death counts for the next four weeks in the U.S. provided by different research teams including ours, through which we can compare our long-term projection with the other methods. It shows that our approach gives reliable guidance of the trend of death in the future.

Table 7.2: Evaluation of one month-ahead prediction.

	D ₁	D ₂	D ₃	D ₄	D ₅	D ₆	D ₇	D ₈	D ₉	D ₁₀
RMSPE	1.86	2.11	2.63	3.41	4.24	4.06	4.41	4.53	4.81	5.45
Coverage	0.97	0.96	0.95	0.94	0.94	0.93	0.92	0.91	0.90	0.90
	D ₁₁	D ₁₂	D ₁₃	D ₁₄	D ₁₅	D ₁₆	D ₁₇	D ₁₈	D ₁₉	D ₂₀
RMSPE	6.08	6.26	6.50	6.82	7.13	7.64	8.17	8.86	9.11	9.32
Coverage	0.89	0.88	0.88	0.87	0.87	0.86	0.86	0.85	0.85	0.84
	D ₂₁	D ₂₂	D ₂₃	D ₂₄	D ₂₅	D ₂₆	D ₂₇	D ₂₈	D ₂₉	D ₃₀
RMSPE	9.52	9.72	9.98	10.58	11.34	11.61	11.89	12.24	12.59	13.01
Coverage	0.84	0.83	0.83	0.82	0.82	0.81	0.80	0.80	0.79	0.79

Note: RMSPE is the daily root of mean squared prediction error for county-level cumulative fatal cases. Coverage is the empirical coverage rate of estimated h -day ahead 95% projection band for county-level cumulative fatal cases.

8 Conclusion and Discussion

This work has aimed to bridge the gap between mathematical models and statistical analysis in the infectious disease study. We created a state-of-art interface between mathematical models and statistical models to understand the dynamic pattern of the spread of contagious diseases. Our proposed model enhances the dynamics of the S(E)IR mechanism through spatiotemporal analysis.

For analyzing the confirmed and death cases of COVID-19, other factors may also be responsible for temporal or spatial patterns. We investigated the spatial associations between the infected count, death count, and factors or characteristics of the counties across the U.S. by modeling the daily in-

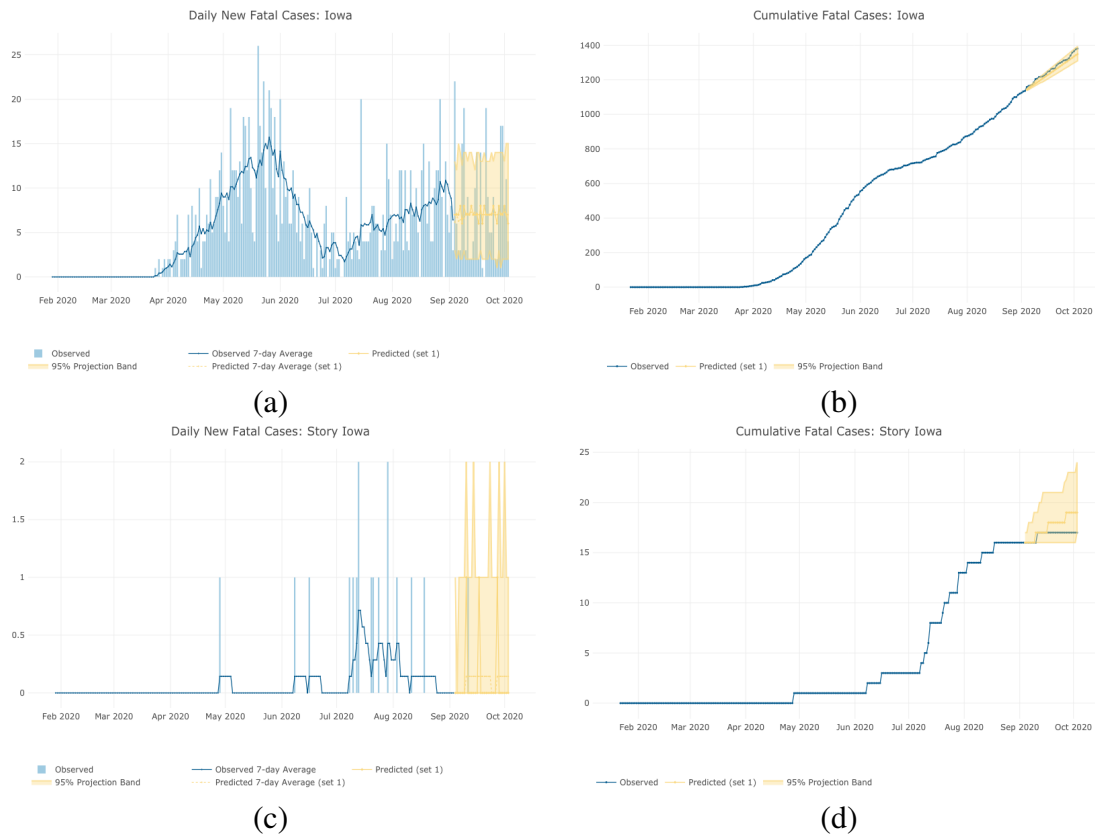


Figure 7.5: Time series plots of new and cumulative fatal cases, and the corresponding projections with 95% prediction bands for the next month in the state of Iowa and Story County, Iowa, based on the observed data 08/26/2020-09/03/2020: (a) new fatal cases in Iowa, (b) cumulative fatal cases in Iowa, (c) new confirmed cases in Story County, Iowa (d) cumulative fatal cases in Story County, Iowa.

fects/fatal cases at the county level in consideration of the county-level factors. Modeling COVID-19 at the county-level and combining local characteristics are very beneficial for the community to understand the dynamics of the disease spread and support decision-making when urgently needed. To examine spatial nonstationarity in the transmission rate of the disease, we proposed a nonparametric spatially varying coefficient model, which allows the transmission to vary from one area to another area. The proposed method can be used as an essential tool for understanding the dynamics of the disease spread, as well as for assessing how this outbreak may unfold through time and space.

Based on our results, disease mapping can easily be implemented to illustrate high-risk areas and thus help policymaking and resource allocation. Our method can also be extended to other situations, including epidemic models in which there are several types of individuals with potentially different area characteristics or more complex models that include features such as latent periods or a more realistic population structure.

Our paper did not take the under-reported issue (for example, the asymptomatic coronavirus infectious cases) into account. Although our model may have partially corrected the problem with the spatiotemporal information, a better way to ultimately solve this problem is to use survey data based on a representative survey sampling strategy Held et al. (2019). For example, following Finkenstädt and Grenfell (2000), we can assume that the true number of confirmed cases (C_{it}^*) is related to the number of reported cases (C_{it}) via $C_{it}^* = \rho_{it}C_{it}$, where ρ_{it} is the reporting rate, and can be estimated based on the survey data. Then, our STEM can be extended further to this scenario.

Data Availability Statement

- A full list of data citations are available by contacting the corresponding author.
- The R package “STEM” of the proposed method can be downloaded from the Github Repository: <https://github.com/covid19-dashboard-us/covid19>.
- The R shiny apps demonstrating the proposed methods can be found from <https://covid19.stat.iastate.edu/>.

Bibliography

- Anastassopoulou, C., Russo, L., Tsakris, A., and Siettos, C. (2020), “Data-Based Analysis, Modelling and Forecasting of the COVID-19 Outbreak,” *PLOS ONE*, 15, 1–21.
- Arab, A., Holan, S. H., Wikle, C. K., and Wildhaber, M. L. (2012), “Semiparametric Bivariate Zero-Inflated Poisson Models with Application to Studies of Abundance for Multiple Species,” *Environmetrics*, 23, 183–196.
- Aratani, L. and Berger, M. (2020), “Here are the 20 U.S. airports where health officials are screening for coronavirus,” Available at <https://www.washingtonpost.com/transportation/2020/01/30/us-health-officials-expand-screening-new-coronavirus-20-airports/>.
- Atlantic (2020), “The COVID Tracking Project Data,” Dataset. Available at <https://covidtracking.com/api>.
- Baud, D., Qi, X., Nielsen-Saines, K., Musso, D., Pomar, L., and Favre, G. (2020), “Real estimates of mortality following COVID-19 infection,” *The Lancet infectious diseases*.
- Brauer, F., Van den Driessche, P., and Wu, J. (2008), *Mathematical Epidemiology*, vol. 1945, Berlin: Springer.
- Cao, G., Yang, L., and Todem, D. (2012), “Simultaneous Inference for the Mean Function Based on Dense Functional Data,” *Journal of Nonparametric Statistics*, 24, 359–377.
- CDC (2020), “CDC Confirms Person-to-Person Spread of New Coronavirus in the United States,” Available at <https://www.cdc.gov/media/releases/2020/p0130-coronavirus-spread.html>.
- CDC (2020), “CDC COVID Data Tracker,” Available at https://covid.cdc.gov/covid-data-tracker/#trends_totalandratecases.

- CDC (2020a), “COVID-19 Forecasts: Cumulative Deaths,” Available at <https://www.cdc.gov/coronavirus/2019-ncov/covid-data/forecasting-us.html>.
- (2020b), “First Travel-related Case of 2019 Novel Coronavirus Detected in United States,” Available at <https://www.cdc.gov/media/releases/2020/p0121-novel-coronavirus-travel-case.html>.
- De Jong, M., Diekmann, O., and Heesterbeek, J. (1995), “How does transmission of infection depend on population size?” *Publications of the Newton Institute*, 5, 84–94.
- Finkenstädt, B. F. and Grenfell, B. T. (2000), “Time Series Modelling of Childhood Diseases: A Dynamical Systems Approach,” *Journal of the Royal Statistical Society, Series C*, 49, 187–205.
- Gog, J. R. (2020), “How You Can Help with COVID-19 Modelling,” *Nature Reviews Physics*, 2, 274–275.
- Gopinath, G. (2020), “The Great Lockdown: Worst Economic Downturn Since the Great Depression,” Available at <https://blogs.imf.org/2020/04/14/the-great-lockdown-worst-economic-downturn-since-the-great-depression/>.
- Held, L., Hens, N., D O’Neill, P., and Wallinga, J. (2019), *Handbook of Infectious Disease Data Analysis*, New York: CRC Press.
- Held, L., Hens, N., O’Neill, P. D., and Wallinga, J. (2020), *Handbook of infectious disease data analysis*, New York: Chapman and Hall/CRC.
- Howard, J. and Yu, G. (2020), “Most People Recover from Covid-19. Here’s Why It’s Hard to Pinpoint Exactly How Many,” CNN News. Available at <https://www.cnn.com/2020/04/04/health/recovery-coronavirus-tracking-data-explainer/index.html>.
- JHU CSSE (2020), “2019 Novel Coronavirus COVID-19 (2019-nCoV) Data Repository,” Dataset. Available at <https://github.com/CSSEGISandData/COVID-19>.
- Jia, J. S., Lu, X., Yuan, Y., Xu, G., Jia, J., and Christakis, N. A. (2020), “Population Flow Drives Spatio-Temporal Distribution of COVID-19 in China,” *Nature*, 582, 389–394.
- Karimi, F. and Moon, S. (2020), “California orders its nearly 40 million residents to stay home to prevent the spread of coronavirus,” Available at <https://www.cnn.com/2020/03/19/us/california-coronavirus-stay-home-order/index.html/>.

- KCRA (2020), “COVID-19: Why patient recovery data is scarce,” Available at <https://www.kcra.com/article/covid-19-questions-recovery-numbers/32093456>.
- Keeling, M. J. and Rohani, P. (2008), *Modeling infectious diseases in humans and animals*, Princeton University Press.
- Kim, M. and Wang, L. (2020), “Generalized Spatially Varying Coefficient Models,” *Journal of Computational and Graphical Statistics*, in press.
- Kong, J., Gu, L., and Yang, L. (2018), “Prediction interval for autoregressive time series via oracally efficient estimation of multi-step-ahead innovation distribution function,” *Journal of Time Series Analysis*, 39, 690–708.
- Kucharski, A. J., Russell, T. W., Diamond, C., Liu, Y., Edmunds, J., Funk, S., Eggo, R. M., Sun, F., Jit, M., Munday, J. D., et al. (2020), “Early Dynamics of Transmission and Control of COVID-19: A Mathematical Modelling Study,” *The Lancet Infectious Diseases*, 20, 553–558.
- Lai, M. J. and Schumaker, L. L. (2007), *Spline Functions on Triangulations*, Cambridge: Cambridge University Press, 1st ed.
- Lai, M. J. and Wang, L. (2013), “Bivariate Penalized Splines for Regression,” *Statistica Sinica*, 23, 1399–1417.
- Lawson, A. B., Banerjee, S., Haining, R. P., and Ugarte, M. D. (2016), *Handbook of Spatial Epidemiology*, New York: CRC Press.
- Liu, R., Yang, L., and Härdle, W. K. (2013), “Oracally Efficient Two-Step Estimation of Generalized Additive Model,” *Journal of the American Statistical Association*, 108, 619–631.
- Liu, W. M., Hethcote, H. W., and Levin, S. A. (1987), “Dynamical Behavior of Epidemiological Models with Nonlinear Incidence Rates,” *Journal of Mathematical Biology*, 25, 359–380.
- Mu, J., Wang, G., and Wang, L. (2018), “Estimation and Inference in Spatially Varying Coefficient Models,” *Environmetrics*, 29, e2485.
- Murray, C. J. et al. (2020), “Forecasting COVID-19 impact on hospital bed-days, ICU-days, ventilator-days and deaths by US state in the next 4 months,” Preprint. Available at [medRxiv:2020.03.27.20043752](https://medRxiv.org/2020.03.27.20043752).

NYT (2020), “Coronavirus (Covid-19) Data in the United States,” Dataset. Available at <https://github.com/nytimes/covid-19-data>.

Phillip Connor (2020), “More than nine-in-ten people worldwide live in countries with travel restrictions amid COVID-19,” Available at <https://www.pewresearch.org/fact-tank/2020/04/01/more-than-nine-in-ten-people-worldwide-live-in-countries-with-travel-restrictio>

Qin, A. and Wang, V. (2020), “Wuhan, Center of Coronavirus Outbreak, Is Being Cut Off by Chinese Authorities,” Available at <https://www.nytimes.com/2020/01/22/world/asia/china-coronavirus-travel.html>.

Sangalli, L., Ramsay, J., and Ramsay, T. (2013), “Spatial Spline Regression Models,” *Journal of the Royal Statistical Society, Series B*, 75, 681–703.

Siettos, C. I. and Russo, L. (2013), “Mathematical Modeling of Infectious Disease Dynamics,” *Virulence*, 4, 295–306.

Staszewska-Bystrova, A. (2009), “Bootstrap Confidence Bands for Forecast Paths,” Available at <https://ssrn.com/abstract=1507451>.

State of Florida, Office of the Governor (2020), “EXECUTIVE ORDER NUMBER 20-51 (Establishes COVID-19 Response Protocol and Directs Public Health Emergency),” Available at https://www.flgov.com/wp-content/uploads/orders/2020/EO_20-51.pdf.

State of the City and County of San Francisco (2020), “Mayor London Breed declares local emergency to prepare for coronavirus,” Available at <https://sf.gov/news/mayor-london-breed-declares-local-emergency-prepare-coronavirus>.

State of Washington, Office of the Governor (2020), “PROCLAMATION BY THE GOVERNOR 20-05,” Available at <https://www.governor.wa.gov/sites/default/files/proclamations/20-05%20Coronavirus%20%28final%29.pdf>.

Sun, H., Qiu, Y., Yan, H., Huang, Y., Zhu, Y., Gu, J., and Chen, S. X. (2020), “Tracking Reproductivity of COVID-19 Epidemic in China with Varying Coefficient SIR Model,” *Journal of Data Science*, 18, 455–472.

TRUMP, D. J. (2020), “Proclamation on Declaring a National Emergency Concerning the Novel Coronavirus Disease (COVID-19) Outbreak,” Available at <https://www.whitehouse.gov/presidential-actions/proclamation-declaring-national-emergency-concerning-novel-coronavirus-disease->

Ujifusa, A. (2020), “States Ordering Schools to Close in Response to Coronavirus,” Available at <https://blogs.edweek.org/edweek/campaign-k-12/2020/03/coronavirus-school-closure-statewide-ohio-first.html/>.

Vespignani, A., Tian, H., Dye, C., Lloyd-Smith, J. O., Eggo, R. M., Shrestha, M., Scarpino, S. V., Gutierrez, B., Kraemer, M. U. G., Wu, J., Leung, K., and Leung, G. M. (2020), “Modelling COVID-19,” *Nature Reviews Physics*, 2, 279–281.

Wakefield, J., Dong, T. Q., and Minin, V. N. (2019), “Spatio-Temporal Analysis of Surveillance Data,” *Handbook of Infectious Disease Data Analysis*, 455–476.

Wang, G., Wang, L., Lai, M. J., Kim, M., Li, X., Mu, J., Wang, Y., and Yu, S. (2019), “BPST: Bivariate Spline over Triangulation,” R package version 1.0. Available at <https://github.com/funstatpackages/BPST>.

Wang, J. and Yang, L. (2009), “Polynomial Spline Confidence Bands for Regression Curves,” *Statistica Sinica*, 19, 325–342.

Wang, L. and Lai, M. J. (2019), “Triangulation,” R package version 1.0. Available at <https://github.com/funstatpackages/Triangulation>.

Wang, L., Liu, X., Liang, H., and Carroll, R. (2011), “Estimation and Variable Selection for Generalized Additive Partial Linear Models,” *The Annals of Statistics*, 39, 1827–1851.

Wang, L., Wang, G., Gao, L., Li, X., Yu, S., Kim, M., and Wang, Y. (2020a), “An R shiny app to visualize, track, and predict real-time infected cases of COVID-19 in the United States,” Available at <https://covid19.stat.iastate.edu/>.

Wang, L., Wang, G., Gao, L., Li, X., Yu, S., Kim, M., Wang, Y., and Gu, Z. (2020b), “An R Shiny App to predict the infected and death cases of COVID-19 in the U.S. in the next two months.” Available at <https://covid19.stat.iastate.edu/longtermproj.html>.

Wang, L., Xue, L., and Yang, L. (2020c), “Estimation of Additive Frontier Functions with Shape Constraints,” *Journal of Nonparametric Statistics*, 32, 262–293.

WHO (2020a), “Coronavirus disease 2019 (COVID-19) Situation Report – 40,” Available at https://www.who.int/docs/default-source/coronaviruse/situation-reports/20200229-sitrep-40-covid-19.pdf?sfvrsn=849d0665_2.

— (2020b), “Pneumonia of unknown cause – China,” Available at <https://www.who.int/csr/don/05-january-2020-pneumonia-of-unkown-cause-china/en/>.

— (2020c), “Timeline: WHO’s COVID-19 response,” Available at <https://www.who.int/emergencies/diseases/novel-coronavirus-2019/interactive-timeline>.

— (2020d), “WHO Director-General’s opening remarks at the technical briefing on 2019 novel coronavirus, 146th session of the Executive Board,” Available at <https://www.who.int/dg/speeches/detail/who-director-general-s-opening-remarks-at-the-technical-briefing-on-2019-novel>

— (2020e), “WHO Director-General’s statement on IHR Emergency Committee on Novel Coronavirus (2019-nCoV),” Available at <https://www.who.int/dg/speeches/detail/who-director-general-s-statement-on-ihc-emergency-committee-on-novel-coronavirus>

Wood, S. N., Pya, N., and Säfken, B. (2016), “Smoothing Parameter and Model Selection for General Smooth Models,” *Journal of the American Statistical Association*, 111, 1548–1563.

Xue, L. and Liang, H. (2010), “Polynomial Spline Estimation for A Generalized Additive Coefficient Model,” *Scandinavian Journal of Statistics*, 37, 26–46.

Yu, S., Wang, G., Wang, L., Liu, C., and Yang, L. (2020), “Estimation and Inference for Generalized Geoadditive Models,” *Journal of the American Statistical Association*, 115, 761–774.

Zheng, S., Liu, R., Yang, L., and Härdle, W. K. (2016), “Statistical Inference for Generalized Additive Models: Simultaneous Confidence Corridors and Variable Selection,” *Test*, 25, 607–626.